Strain partitioning and exhumation in oblique Taiwan collision : role of rift architecture and plate kinematics

Clément Conand, Frédéric Mouthereau, Jérome Ganne, Andrew Tien-Shun Lin, Abdeltif Lahfid, Maxime Daudet, Lucas Mesalles, Slawek Giletycz, Marta Bonzani

AGU ADVANCING EARTH AND SPACE SCIENCE

Tectonics

RESEARCH ARTICLE
10.1029/2019TC005798

Special Section:
Collisional orogenic systems as recorders of collisions between arc and continents

Strain Partitioning and Exhumation in Oblique Taiwan Collision: Role of Rift Architecture and Plate Kinematics

Clément Conand[1], Frédéric Mouthereau[1,2], Jérome Ganne[1], Andrew Tien-Shun Lin[5,2], Abdeltif Lahfid[3], Maxime Daudet[1], Lucas Mesalles[4], Slawek Giletycz[5], and Marta Bonzani[1]

[1]Geosciences Environnement Toulouse, Université de Toulouse 3, Université Paul Sabatier, CNRS, IRD, Toulouse, France, [2]LIA D3E "From Deep Earth to Extreme Events," CNRS-MOST, Taipei, Taiwan, [3]Bureau de Recherches Géologiques et Minières, Institut des Sciences de la Terre d'Orléans, Orleans, France, [4]Department of Earth and Environment Sciences, National Chung-Cheng University, Chiayi, Taiwan, [5]Department of Geophysics, National Central University, Chungli, Taiwan

Abstract Taiwan is an archetypal example of continental accretionary wedges. Yet the generally poor knowledge of three-dimensional strain distribution over time and role of architecture of the rifted margin shed doubt on the cylindrical two-dimensional kinematic models of Taiwan collision. Here we provide new field-based constraints on strain distribution, new Raman Spectroscopy on Carbonaceous Materials temperatures and apply mica-chlorite multiequilibrium approach to determine pressure-temperature in the Central Range of Taiwan. We identify three distinct structural domains that define zones of orthogonal shortening in the western Backbone Range and left-lateral ductile shearing overprinted by left-lateral transtensional brittle deformation in eastern Central Range. Field surveys show the lack of nappe stacking in the Backbone Range. Combining new temperature estimates with existing thermochronological constraints we emphasize that western Taiwan mostly inherited preorogenic thermal history. We show that metamorphic peak conditions of 5–6 kbar and 330–400 °C in the eastern Backbone Range and HP rocks of the Yuli Belt exhumed along the *P-T* paths related to transcurrent deformation. We propose a three-dimensional kinematic model of Taiwan accounting for the oblique motion of the Philippine Sea Plate relative to the plate boundary and the reactivation of a NS striking transform fault in the South China Sea rifted margin. Recent and ongoing strain partitioning in the Taiwan accretionary wedge is reflected by the coexistence of brittle left-lateral shear, oblique extension, and contraction. Our results have impact on orogen-based plate kinematic reconstructions that consider two-dimensional kinematic evolution of orogens.

Key Points:
- Strain distribution in south central Taiwan reveals partitioning between orthogonal contraction and left-lateral shear
- Dome-like architecture and exhumation of high-grade rocks in eastern Taiwan are best explained by transcurrent deformation
- Oblique convergence and rift architecture accounts for the 3-D strain distribution in Taiwan

Supporting Information:
- Supporting Information S1

Correspondence to:
C. Conand,
conandclement@hotmail.fr

Citation:
Conand, C., Mouthereau, F., Ganne, J., Lin, A. T.-S., Lahfid, A., Daudet, M., et al. (2020). Strain partitioning and exhumation in oblique Taiwan collision: Role of rift architecture and plate kinematics. *Tectonics*, *38*. https://doi.org/10.1029/2019TC005798

Received 31 JUL 2019
Accepted 22 FEB 2020
Accepted article online 12 MAR 2020

1. Introduction

Taiwan is the result of the oblique collision (Figure 1) between the ENE striking northern South China Sea (SCS) rifted margin and the NS directed Luzon Arc (Dahlen, 1990; Davis et al., 1983; Suppe, 1981). Its structure is interpreted to be the product of WNW-ESE accretion of SCS materials, orthogonal to the strike of the orogen, through a series of thrusts rooting at middle crustal level in a low-angle main thrust detachment (Crespi et al., 1996; Dahlen, 1990; Davis et al., 1983; Malavieille, 2010; Simoes et al., 2007; Suppe, 1981). In this view, the increasing eastward crustal thickening and tectonic burial explains metamorphism of SCS marginal units that experienced upper greenschist to blueschist facies now exposed in the Central Range (Barr et al., 1991). Well-documented high exhumation rates (3–6 km/Myr) reflect interactions between tectonics and surface processes, modulated by climate (Dadson et al., 2003; Hovius et al., 2000; Willett, 1999). The pattern of focused rapid exhumation and lack of present-day and recent surface shortening in the eastern Central Range have been interpreted to reflect aseismic nappe stacking by ductile duplexing and underplating has been inferred to take place (Chen et al., 2011; Clark et al., 1993; Malavieille, 2010; McIntosh et al., 2013; Simoes et al., 2007; Suppe, 1981). Such a tectonic model reproduces well the patterns of thermochronological ages and distribution of metamorphic facies across Taiwan (Willett et al., 2003; Fuller et al., 2006). Another important feature of the strain field in the Central Range is depicted by the orogen-(near)parallel extension documented by geodesy, and earthquake focal mechanisms (Chang et al., 2000; Lin, 2002; Mouthereau et al., 2009). When combined with recent fault patterns and principal strain

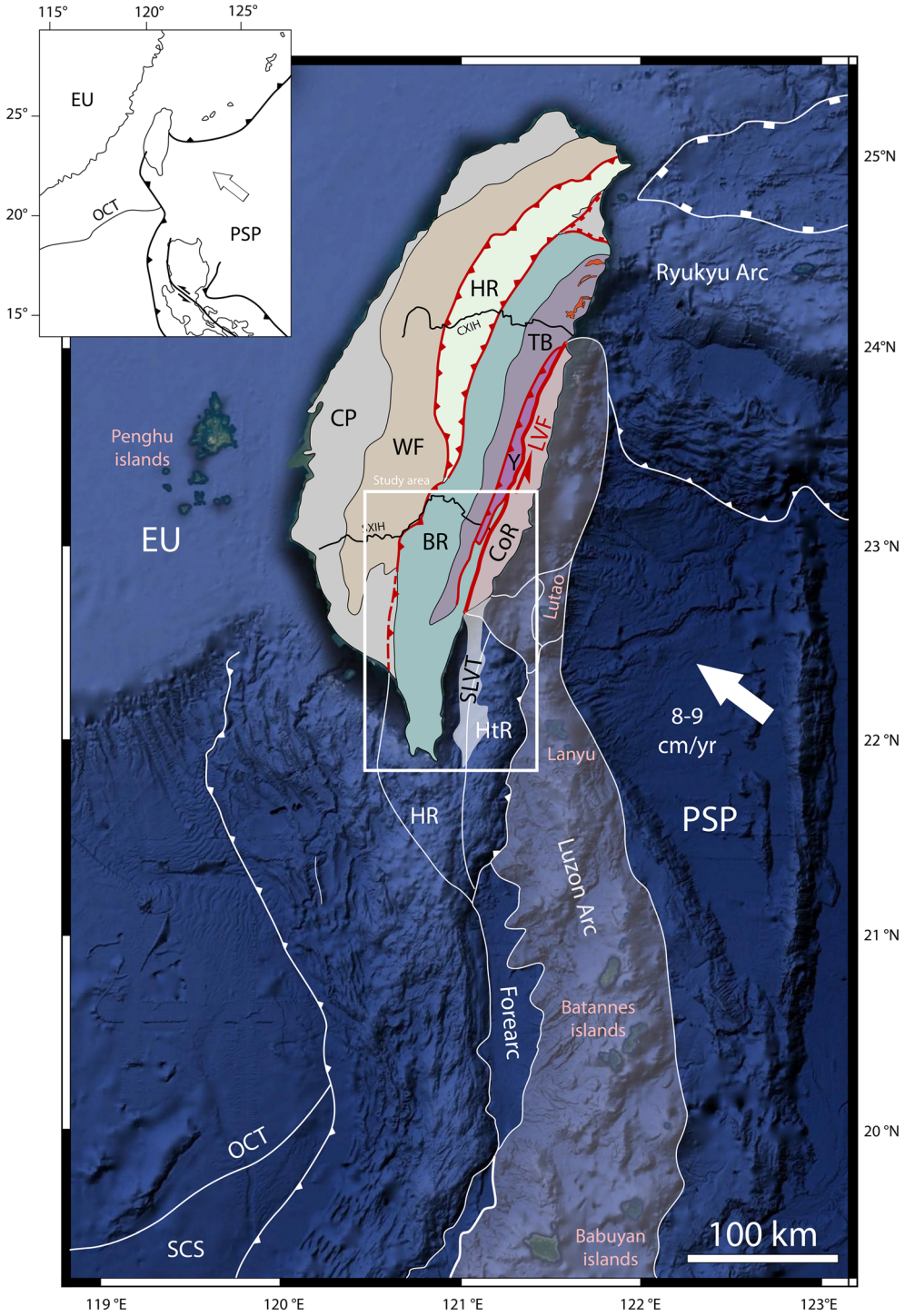

Figure 1. Geological and kinematic setting of Taiwan arc-continent collision. Abbreviations: EU, Eurasian plate; PSP, Philippine Sea Plate; OCT, Ocean-Continent Transition; SCS, South China Sea; CP, Coastal Plain; WF, Western Foothills; HR, Hsuehshan Range; BR, Backbone Range; TB, Tailuko Belt; Y, Yuli belt; CoR, Coastal Range; CXIH, Central Cross-Island Highway; SXIH, Southern Cross-Island Highway; HR, Hengchun Ridge; HtR, Huatung Ridge; SLVT, South Longitudinal Valley Through. Granitic gneiss exposed in the northern Tailuko Belt are shown. Offshore domains and faults are from Malavieille and Trullenque (2009).

axes, a consistent strike-slip regime with nearly E-W shortening is also defined associated with normal faulting (Mouthereau & Lacombe, 2006 among others). The present-day strain pattern further agrees with ductile strain analyses in the Central Range showing orogen-parallel stretching and left-lateral strike-slip shearing

(e.g., Fisher et al., 2002; Pulver et al., 2002; Tillman & Byrne, 1995). The homogeneous two-dimensional strain field assumed by the tectonic wedge model therefore fails to explicitly reproduce the simultaneous contraction, extension, and transcurrent deformation pattern in Taiwan, where boundary kinematic conditions are obviously three-dimensional, as expected in obliquely convergent margins (e.g., Teyssier et al., 1995). The noncylindricity of the range should therefore be significant, a feature that is not retrieved in the current tectonic map of Taiwan or structural interpretation.

Strain distribution in orogens are also known to be dependent on the architecture of the accreted rifted margin (e.g., Jourdon et al., 2019). For instance, seismic data offshore suggest that Taiwan incorporates the variably thinned crust of the SCS rifted margin (Lin, 2000; Franke et al., 2014; Eakin et al., 2014; Gozzard et al., 2019), which geometry may explain some first-order features of the exhumation pattern (Byrne et al., 2011). The major part of structural studies dealing with brittle and ductile deformation in Taiwan have been conducted in the central part of Taiwan where the deepest crustal levels are exposed. By contrast, the tectonics of the earliest stages of the collision as observed in southern Taiwan has only been scarcely explored (e.g., Pelletier et al., 1986). How tectonic motions are partitioned between upper and lower crustal levels in space and time is therefore unresolved.

To fill this gap we provide an integrative, field-based study of the deformation in the internal domain of southern Taiwan at the transition between subduction (and initial continental accretion) and collision (or mature arc-continent collision). This is combined with Raman Spectroscopy on Carbonaceous Materials (RSCM) analyses of maximum temperature and new pressure-temperatures of low-grade metamorphic slates of central Taiwan based on phengite-chlorite multiequilibrium.

We show that ductile and brittle deformation across Taiwan displays a consistent pattern that reveals the progressive increase of strain localization eastward accommodated by left-lateral strike-slip shear. These results indicate that the obliquity of the plate convergence relative to the strike of the belt is partitioned between a component of frontal accretion orthogonal to the belt, and a wide zone of brittle and ductile left-lateral shear at the rear. The observed pattern of transcurrent deformation is consistent with the reactivation of a NS striking transform fault since 15 Ma. On the other hand, the gravitational stresses at the origin of the extension are likely controlled by the bathymetry of the rifted margin. The north directed transport of deep-seated units of the metamorphic belt east of the orogenic wedge has strong impact on the geophysical interpretation of the crustal root, and plate kinematic reconstructions that implicitly consider two-dimensional structure.

2. Geodynamic and Geological Setting

2.1. Current and Past Plate Kinematics of Taiwan Collision

Taiwan results from the collision between the northern SCS rifted margin and the Luzon arc (Figure 1). The N110° trending and fast convergence (~8 cm/year) between Eurasia and the Philippine Sea Plate is oblique to the direction of the Chinese rifted margin trending ENE (e.g., Yu et al., 1997). This unique setting allows examination of mountain building processes at different stages of collision maturity from submarine continental accretion of south Taiwan (20°–22.5°N), mature collision stages with high topography in central Taiwan (22.5°–24°N), and postorogenic back-arc extension in northern Taiwan and the Okinawa Through (>24°N) as a result of subduction polarity reversal (Angelier, 1990; Clift et al., 2008; Letouzey & Kimura, 1986; Sibuet et al., 1987; Suppe, 1981; Teng, 1996).

The transition from oceanic subduction of the SCS at the Manilla trench to initial continental accretion is observed 100 km off southern Taiwan at approximately 20°N (Figure 1). Seismic reflection profiles and tomography indeed provided images of the SCS hyperextended margin with synrift basins and a distinctive breakup unconformity just west of the deformation front of the submarine accretionary wedge (Eakin et al., 2014; Lester et al., 2013; McIntosh et al., 2013; Wang & Hu, 2006; Zhao et al., 2010). From 22.5°N northward, the arc-continent collision is defined by the presence of the Lichi mélange, stretching along the southern half of the Longitudinal Valley Fault (Chang et al., 2001; Ho, 1986; Huang et al., 2008; Huang et al., 2018; Jahn, 1986; Page & Suppe, 1981; Shellnutt & Hsieh, 2016) that resulted from the consumption of the forearc oceanic basement between the Luzon Arc and the accreted Eurasian margin (Figure 1).

The initiation of continental accretion occurred 6–7 Myr ago. This is indicated by the onset of flexural loading in the western Taiwan foreland (Lin et al., 2003) and onset of cooling recorded in prerift and late synrift/postrift Miocene deposits of the SCS passive margin (Mesalles et al., 2014). Successive phases of increased exhumation rates are described at 5, 2–1.5, and 0.5 Ma (Hsu et al., 2016; Lee et al., 2015; Mesalles et al., 2014). Mountain building eventually reached an erosional steady-state but has likely been achieved only recently. The punctuated growth of the Taiwan mountains likely reveals complex interrelationships between the architecture of the accreted SCS margin, indentation, and accretion of the Luzon arc/forearc as well as changes in the erosional patterns and plate kinematics.

Plate reconstructions of the Philippine Sea plate suggest that subduction of the South China Sea began approximately 15 Myr ago and was directed NNW-SSE at high angle (almost 80° of obliquity) with the NS striking orientation of the subduction trench (e.g., Wu et al., 2016). This timing is consistent with the formation of the East Taiwan ophiolite at 15 Ma when the SCS spreading axis or near-ridge seamount was incorporated in the Lichi mélange (Chung & Sun, 1992; Huang et al., 1979; Jahn, 1986; Suppe, 1981) and by the age of onset of arc volcanism in the Coastal Range at 16–15 Ma (e.g., Huang et al., 2006). This is further supported by the age of the collision of the Mindoro-Palawan block of Eurasian affinity with the Western Philippines (e.g., Sarewitz & Karig, 1986; Marchadier & Rangin, 1990; Pubellier et al., 2003; Yumul et al., 2003). It is also temporally correlated within error to the cessation of spreading in the South China Sea between 20.5 and 15 Ma (Barckhausen et al., 2014; Briais et al., 1993; Li et al., 2014). The oblique convergence between the EU and PSP implies strain partitioning into components of shortening perpendicular to the subduction front and left-lateral strike-slip faulting that is accommodated along the Philippine Fault (e.g., Barrier et al., 1991; Pinet & Cobbold, 1992; Pinet & Stephan, 1990) and is likely continuing northward into Taiwan. Left-lateral strike-slip faulting is indeed described along the active Longitudinal Valley Fault (e.g., Lee et al., 1998; Shyu et al., 2005; Shyu et al., 2006, 2008).

2.2. Main Tectonic Divisions, Metamorphism, and Brittle/Ductile Deformation Patterns

2.2.1. Tectono-Metamorphic Units

Taiwan is typically divided into several tectonic units (Figures 1 and 2). The Coastal Range to the east represents the northern Luzon Arc accreted to the collided margin. The Longitudinal Valley Fault is the plate boundary fault between the Coastal Range and the Central Range, along which the Lichi mélange is exposed (Chang et al., 2000; Ho, 1986; Huang et al., 2018; Jahn, 1986; Lin et al., 2019). The metamorphic core of the Central Range comprises two metamorphic units: the Tailuko Belt (TB) and the Yuli Belt (YB). The TB is composed of Paleozoic to Mesozoic slates with Eurasian affinity, including in the northern Taiwan marble layers and foliated Cretaceous granitic intrusions dated at 85–90 Ma (Figure 1; Jahn, 1986; Lo & Onstott, 1995; Wintsch & Li, 2014). This unit is overprinted by a HT metamorphism that is not only due to those granitic intrusion. RSCM analyses indicate maximum temperature of 350–550 °C (Beyssac et al., 2007). Independent *P-T* constraints from the Chipan gneiss show peak metamorphism (T = 500 °C and P = 6–8 kb) in accordance with predicted tectonic paths (Barr & Dahlen, 1989; Simoes et al., 2007). One fully reset Ar40/Ar39 age obtained on biotite indicate that these rocks rapidly exhumed by 7–8 Ma (Lo & Onstott, 1995). The YB is dominated by slaty country rocks which ages have been recently determined to be middle Miocene (Chen et al., 2017; Mesalles et al., 2019). The occurrence of blueschist metamorphism is documented by glaucophane and omphacite-bearing rocks retrieved from mafic/ultramafic exotic blocks (Figure 2). Peak metamorphic conditions yielded temperatures of about 486–550 °C and pressures of 7–17 kbar (Baziotis et al., 2017; Beyssac et al., 2007; Beyssac et al., 2008; Keyser et al., 2016; Tsai et al., 2013). These conditions have been reached between 16 Ma (depositional age determined by zircon U-Pb dating; Chen et al., 2017) and 12 Ma as derived by Ar40/Ar39 dating on amphibole, phengite, and phlogopite (Lo & Yui, 1996). The TB is overlain by slates formed by synrift shallow-marine Eocene deposits and postrift Miocene deep-marine sediments of the Backbone Range (BR). The Eocene slates are composed of phyllite with interbeds of metasandstones/conglomerates and limestones while the Miocene slates are made of argillite with thin layers of sandstones and metasandstones (Ho, 1986; Chen et al., 1983a; Fisher et al., 2002). These sediments have been metamorphosed under lower greenschist metamorphic conditions (T = 300 ± 50 °C, P = 4 kb; Liou & Ernst, 1984).

In the Hsuehshan Range (HR) a thick sequence of synrift Eocene and Oligocene shallow-marine sedimentary sandstones and conglomerates of the Pilushan formation are resting unconformably on top of the

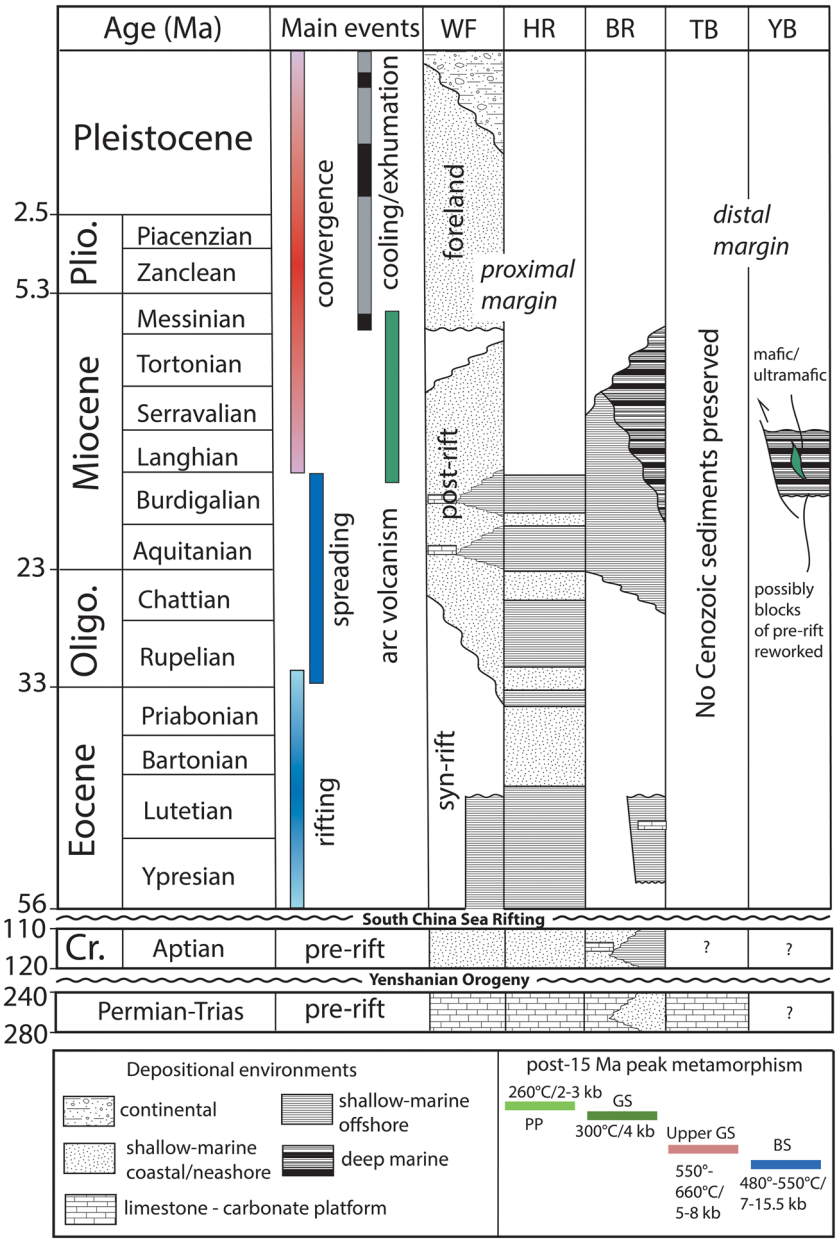

Figure 2. Tectono-stratigraphic chart of Taiwan with a focus on post-Eocene sedimentary rocks and inferred position of the different domains along the South China Sea paleomargin. Compilation after Teng et al. (1991), Lin et al. (2003), and Ho (1986).

pre-Cenozoic Mesozoic to Paleozoic basement of Central Taiwan (e.g., Ho, 1986; Figure 2). The sediments have been slightly metamorphosed at prehnite–pumpellyite to lower greenschist facies (T = 260 ± 40 °C, P = 2–3 kb; Liou & Ernst, 1984).

The southernmost occurrence of Eocene rocks dated by fossil occurrence is within the BR (e.g., Ho, 1986) at the southern tip of Taiwan at roughly 22.4°N. To the south, the Hengchun Peninsula hosts the southern continuation of the BR made with middle-late Miocene sediments and the Kenting ophiolitic mélange, containing exotic igneous blocks of late Oligocene ages of 22–26 Ma with affinity from the SCS (Pelletier et al., 1985; Pelletier & Stephan, 1986; Zhang et al., 2016). The western nonmetamorphic fold-and-thrust belt, namely, the Western Foothills, is made of foreland and rifted margin deposits accreted to the growing orogenic wedge during the Pliocene. Further west, the Coastal Plain lies at the transition between the frontal thrust units and the western foredeep (Figure 1).

2.2.2. Strain Distribution and Evidence for Strain Partitioning

Microstructural analyses show that the kinematics of Taiwan is partitioned between a component of lateral and orogen-perpendicular deformation due to the obliquity of the convergence (e.g., Pulver et al., 2002). In western Taiwan, axial planar steeply dipping cleavages in HR reflect a coaxial strain history and pure shear shortening (Fisher et al., 2002; Tillman & Byrne, 1995). The low magnitude of ductile strain in the HR compared to prediction of critical wedge model (Clark et al., 1993) is interpreted to reflect strain localization along out-of-sequence thrusts (Clark et al., 1993) or underplating (Beyssac et al., 2007; Simoes et al., 2007) but could also indicate some degree of strain partitioning as suggested by Pulver et al. (2002). Likewise the HR, the western BR is characterized by top-to-the-west shear structures, including NE trending fold axes, and cleavage (Huang & Byrne, 2014; Tillman & Byrne, 1995). Stretching lineations throughout are downdip and associated with fibrous elongate chlorites-phengite aggregates (Fisher et al., 2002). The orogen-perpendicular deformation that prevails in HR and western BR contrasts with strain pattern documented in the metamorphic core of northeastern Taiwan. Indeed, the pre-Tertiary basement, including granitic gneiss (Chipan gneiss), shows a penetrative fabric S1 oriented NE with a shallowly plunging stretching lineation L1 defined by greenschist mineral assemblage. Kinematic analysis shows that the pre-Tertiary metamorphic basement is dominated by noncoaxial, constrictional deformation, left-lateral strike-slip motion with a normal sense of shear increasing toward the east (Pulver et al., 2002). The Eocene formation of eastern part of the Backbone Range shows consistent noncoaxial strain outlined by stretching lineations parallel to the NE plunges of fold axes. This ductile fabric is intersected by west dipping brittle normal-fault zones and veins that are associated to active hot springs (Fisher et al., 2002). Deformation pattern in eastern Taiwan therefore agree with a kinematic model in which the oblique convergence is partitioned between NW shortening and orogen-parallel strike-slip motion.

2.3. The South China Sea Rifted Margin Evolution in Taiwan

Figure 2 summarizes the main tectonic and stratigraphic features of Taiwan. Seismic data and subsidence analysis of deep wells in the proximal margin off western Taiwan (Lin et al., 2003) show that rifting of the SCS margin initiated during the Paleogene (58–37 Ma). The synrift late Paleocene sediments accumulated in shallow-marine to continental environment. These sediments unconformably overlie the Yenshanian basement composed of Permian-Triassic metasediments (mostly marbles) topped by early Cretaceous (Aptian) slates. By 37 Ma, the focus of rifting shifted to the present-day OCT boundary off southern Taiwan (Lin et al., 2003; Figure 1). The onset of continental breakup and initial seafloor spreading in the South China Sea is dated between ~31 Ma (Chron C12n) and 29.5 Ma (Chron C11) according to the oldest magnetic anomalies (Briais et al., 1993; Franke, 2013; Li et al., 2014). Seafloor spreading then propagated from NE to SW at ~23 Ma (Briais et al., 1993; Li & Song, 2012; Li et al., 2012; Franke, 2013). Early postbreakup subsidence (30–18 Ma) is recorded by fluvial-to-marine successions in Taiwan area on the proximal rifted margin (Lin et al., 2003). This contrasts with the outer rifted margin where thick Oligocene-Miocene, mainly marine, postbreakup succession (e.g., Tainan basin) is bounded by a seaward dipping fault (Lin et al., 2003). The variable postbreakup subsidence histories illustrate the coexistence of complex thermal and fault-controlled subsidence in the proximal and distal SCS rifted margins associated with postbreakup uplift at 12.5 Ma. The large crustal thinning on the distal margin agrees with geological evidence in southern Taiwan (Hengchun Peninsula) that synrift/prerift Mesozoic to Oligocene lithologies are lacking but are overlain by several kilometers of deep water, essentially postbreakup Miocene "flysch" sediments (Pelletier, 1985; Giletycz et al., 2015; Zhang et al., 2016).

3. Methods and Sampling Strategy

This study focuses on the slate and schist belts of southern Taiwan between 21.9°N and 23.3°N at the transition between the incipient collision in the Hengchun Peninsula to mature collision in central Taiwan (Figures 1 and 3). We targeted several E-W transects in order to study the deformation pattern across the contact between low-metamorphic-grade Miocene flysch units (including Eocene sandstones) of the southern Backbone Range and high-metamorphic-grade units of the Tailuko Belt and Yuli Belt. Because outcrops are only accessible in rivers, we selected E-W valleys on the eastern and western sides of the belt in which exploration can be made as deep as possible in the mountain belt. Structural data on ductile and brittle

deformation were collected providing an unprecedented database (Figure A1). We collected oriented samples in all the studied valleys for microstructural observations, RSCM, and Chlorite thermometry and thermo-barometry estimates on metapelites based on phengite-chlorite equilibrium. Those results combined with existing low-temperature thermo-chronology constraints allow identifying the structural domains of the slate and schist belts. We aimed at resolving (1) the structural position of the Backbone Range (Miocene-Eocene slates and metasandstones) that is regarded as being allochthonous or parautochthonous relative to the Tailuko and Yuli Belts, depending on the thin-skinned or thick-skinned two-dimensional tectonic models (e.g., Malavieille & Trullenque, 2009; Yamato et al., 2009) and (2) the relative importance of brittle and ductile strike-slip movements across Taiwan relevant to define whether the strain history is two-dimensional or three-dimensional.

To determine peak temperature reached by sediments in southern Taiwan, we performed RSCM on Miocene-Eocene pelitic rocks. Sixty-six samples were collected in the study area and the major part is located along selected transects in western and eastern Taiwan (Figure 3). The RSCM study was used to quantify the degree of thermal transformation of carbonaceous materials. This process is an irreversible process. Thus, RSCM data represent the maximum temperature reached during sedimentary or tectonic burial and metamorphic event(s). RSCM analyses were performed at the Bureau de Recherches Géologiques et Minières in Orléans using the Renishaw inVia Reflex system with a light source of a 514-nm Spectra Physics argon laser. Renishaw WiRE 3.4 was used for spectrometer calibration and Raman measurements (e.g., Delchini et al., 2016). Four to 23 particles of carbonaceous materials (with an average of 16.4 for all samples) were analyzed per sample. Standard errors are given for temperature with 1σ. Temperatures between 330 and 640 °C were estimated using the calibration of Beyssac et al. (2002). For lower temperatures (200–330 °C), we have applied the extended calibration of Lahfid et al. (2010).

Chlorite-phengite-quartz-H_2O multiequilibrium thermobarometry was conducted for samples 17-37, 17-39, 17-40, and CSC10, which are characterized by occurrences of coprecipitated chlorite and muscovite assemblages. Chemical compositions on different mineral phases were performed at the Centre for Microanalyses Raymond Castaing (Université Paul Sabatier) using a CAMECA SXFive Electronic microprobe. The accelerating voltage was 15 kV for a beam current of 10 or 20 nA corresponding to an analyzed surface of 2 × 2 μm^2. To estimate *P-T* conditions with chlorite-phengite couples and thermometry on chlorites and amphibole, those data were combined with whole-rock analyses realized by the SARM center in Nancy, using ICP-AES analyses for major elements and ICP-MS analysis for trace elements. Multiequilibrium calculations were performed with Matlab© and using the latest thermodynamic model for phengite (Dubacq et al., 2010), which takes into account the *T*-dependent interlayer water content of dioctahedral phengite. *P-T* estimates for the chlorite, phengite, quartz, and water parageneses were calculated using the thermodynamic data of five chlorite and six phengite end-members. These end-members are Fe amesite (FeAm: $Si_2Al_4(Fe)_4O_{10}(OH)_8$), Mg amesite (MgAm: $Si_2Al_4(Mg)_4O_{10}(OH)_8$), clinochlore (Clin: $Si_3Al_2Mg_5O_{10}(OH)_8$), daphnite (Daph: $Si_3Al_2Fe_5O_{10}(OH)_8$), and sudoite (Sud: $Si_3Al_4(Mg,Fe)_2O_{10}(OH)_8$) for chlorite, and muscovite (Ms: $Si_3Al_3KO_{10}(OH)_2$), pyrophyllite (Prl: $Si_4Al_2O_{10}(OH)_2$), hydrated pyrophyllite (Prl.H_2O: $Si_4Al_2O_{10}(OH)_2.H_2O$), Fe celadonite (FeCel: $Si_4Al(Fe)KO_{10}(OH)_2$), Mg celadonite (MgCel: $Si_4Al(Mg)KO_{10}(OH)_2$), and phlogopite (Phl: $Si_3AlMg_3KO_{10}(OH)_2$ for phengite. Among the 359 equilibria that can be written for the Chl-Phg-Qtz-water assemblage, seven are independent. The *P*, *T* of equilibrium between Chl, Phg, Qtz, and the Fe_3^+ content in chlorite and phengite and the water content of phengite were calculated in order to minimize the sum of the Gibbs free energy $\sum \Delta G^2$ of the following seven independent reactions:

1. 1 Sud + 15 Qtz + 10 FeCel + 2 MgAm --> 4 Prl + 10 MgCel + 2 Daph
2. 6 MgCel + 7 Qtz + 4 FeAm + 4 H2O --> 6 FeCel + 3 Sud + 2 Daph
3. 5 MgAm + 4 Daph --> 5 FeAm + 4 Clin
4. 14 Qtz + 5 FeAm + 3 MgAm + 8 H2O --> 4 Daph + 6 Sud
5. 2 Sud + 4 Qtz + 4 Daph + 4 Ms --> 2 PrlH + 4 MgCel + 5 FeAm
6. 1 Prl + 1 H2O --> 1 PrlH
7. 11 Qtz + 2 Ms + 1 Phl + 2 H2O --> 3 MgCel + 2 Prl

In theory, thermodynamic equilibrium is achieved for a given couple if $\sqrt{(\sum \Delta G^2/nr)}$ is equal to 0. In practice, a deviation from 0 occurred because of analytical uncertainties. After Monte Carlo simulations

accounting for the analytical uncertainties, equilibrium is considered to be achieved when $\sqrt{(\sum \Delta G^2/nr)} < 2{,}400$ J for the conventional point analyses. *P-T* uncertainties ($\pm 2\sigma$) are estimated to ± 0.8 kbar/± 10 °C for point analyses (Ganne et al., 2012).

4. Structural Analyses

Field work missions were carried out in southern part of Taiwan on the Miocene postrift and Eocene synrift formations exposed in the Backbone Range, Tailuko and Yuli Belt, south of the southern cross-island highway (Figure 3). About 200 sites were visited in 18 EW directed valleys. The analyses of brittle and ductile deformation led us to identify three structural domains that are described below.

4.1. Structural Domain I

Domain I is defined by axial-planar, SE dipping slaty cleavages S1 and west vergent folds of variably metamorphosed, mainly Miocene, flysch series (Figures 3–5). This domain stretches between the western Backbone Range and its continuation in the Hengchun Peninsula. Relationships between bedding (S0) of Miocene series and slaty cleavages (S1) is often obvious (Figure 5).

The SE dipping cleavage S1 (Figure 4c) is oriented N-S to NNE-SSW, except very locally, few kilometers north of Wutai Valley, near Paolai, where S1 is turning almost E-W (Figure 4c). S1/S0 relationships show kilometer-scale west vergent folding with overturned limbs cut by a few top-to-the-NW thrust faults next to the Chaochou Fault with relatively minor displacement (mesoscale faulting), indicating a small component of localized shear (see cross sections A-A′ and B-B′ in Figure 6).

Fault slip data reveal a WSW-ENE (Sites 83, 94) and SSW-NNE (Site 86) extension. Near the bend of the Chaochou Fault, an oblique NNW-SSE to NNE-SSW compression (Sites 92, 96) is locally resolved (Figure 7). Wherever documented, reverse or normal faulting postdates or is synchronous with folding (bedding-parallel shear). From north to south, the changing nature of S1, ranging from slaty cleavages (Figure 5b) in the north to pencil cleavages and lack of ductile deformation in the Hengchun Peninsula (Figure 5c), reveal that deformation occurred at temperature from 300 °C in the north to below 200 °C southward. The zonation of cleavage type outlines a dome-like structure, mimicking the regional antiformal structure of the Central Range. Because spatial distribution of cleavages is also correlated with deeper structural units to the north, the inferred temperature pattern may be related to the original stratigraphic position. In Wutai and Maija Valleys, the boundary between the Miocene slates and Eocene slates and metasandstones/conglomerates is seen to be continuous, devoid of major shear zones, consistent with the observation of similar S1 attitude and style of deformation (Figure 4). Structural relationships therefore indicate that the contact between postrift Miocene and synrift Eocene strata is stratigraphic in origin and was later tectonically buried and folded during the collision.

4.2. Structural Domain II

By contrast with domain I, domain II is defined by SW dipping S1 and well-defined N-S to NW-SE left-lateral normal faults (Figures 4 and 8). It lies on the eastern flank of the Backbone Range, close to the contact with the pre-Tertiary basement (Figure 3). Located in the slaty cleavage zone, the bedding S0 can occasionally be observed thanks to metasandstone alternations, allowing for determination of bedding polarities. Distinctive near-flat S0 and S1 planes are found in the easternmost part of the Taimali section (cross section C-C′ in Figure 8). To the west of Taimali and throughout Chihpen S1 is trending N-S and is essentially SW dipping (Figure 4c).

The change in S1 geometry, including a kilometer-scale area with west dipping S1 (e.g., Taimali Valley; Figure 8), is seen to occur across N-S to NW-SE striking left-lateral normal faults (Figure 7; sites 215, 222, 223, 231, 237, 239, 247, 249). Those brittle features define a transtensional domain consistent with a prominent WSW-ENE to SSW-NNE extension, which is remarkably homogeneous throughout the area. Most faults are W to SW dipping and cut through S1 and S0 folds. The stretching lineation L1 (Figure 4d) formed by oriented crystallization of phengites and/or chlorites, parallel to stretched and truncated pyrites or elongate pebbles (Figures 9a and 9b), aligned with fold axes, altogether define an elongation oriented SSW-NNE slightly oblique to the brittle extension defined above (Figures 5 and 9c–9f). To the north, near the contact with the metamorphic basement in the Chihpen Valley, noncoaxial strain seems to increase as suggested

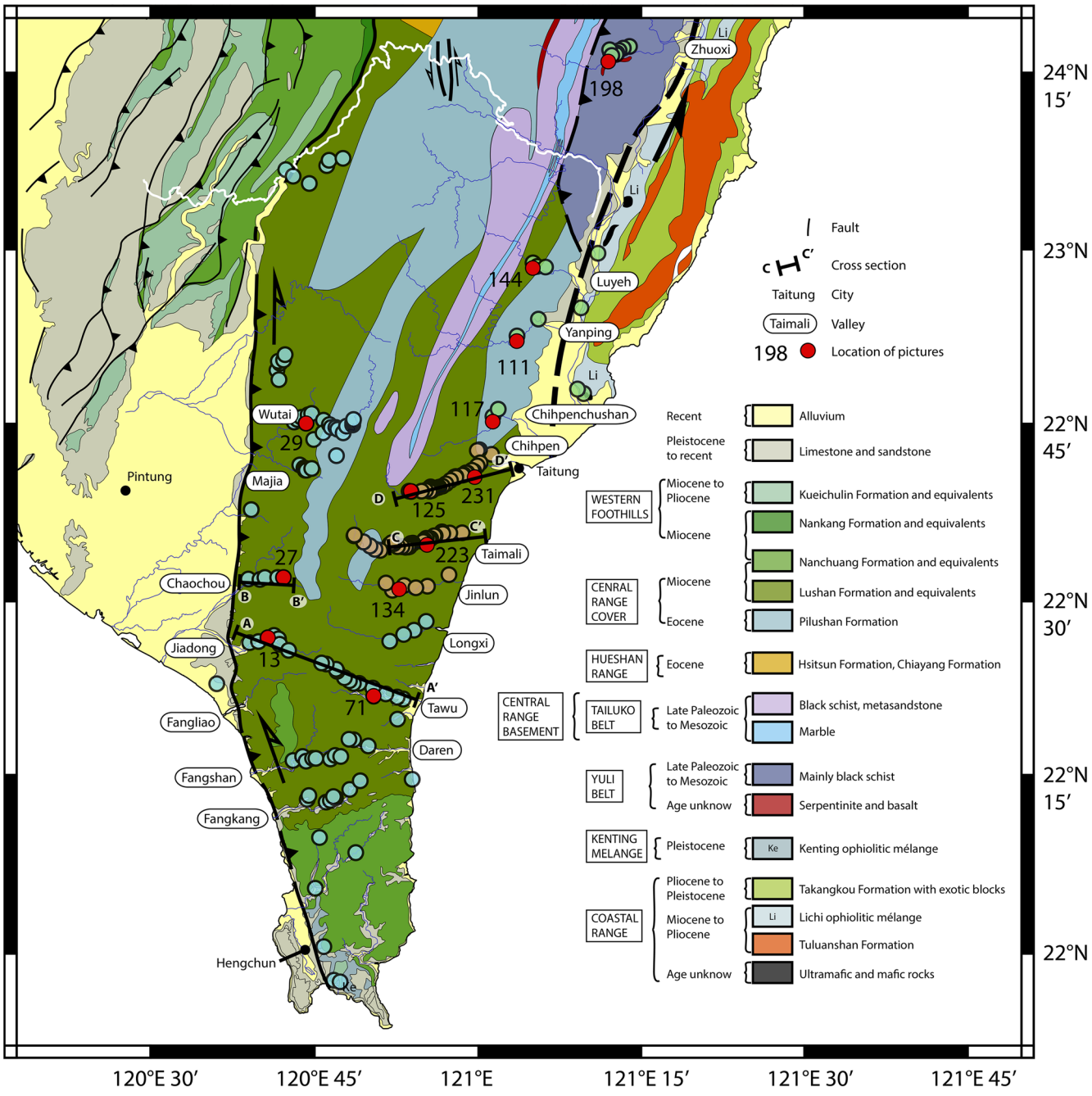

Figure 3. Geological map of south-central Taiwan and Hengchun Peninsula. Sites visited are indicated by colored circles. The colors refer to the structural domains I, II, and III mentioned in the text. Names of valleys explored in this study are also indicated.

by asymmetric boudinage of S0/S1 layers, pressure shadows around quartz nodules at microscale, and S/C structures with dominant normal top-to-the SW sense of shear. The contact between Miocene and the metamorphic basement of the Tailuko and Yuli Belt show no evidence of a major shear zone or a marked increase in the metamorphic grade. This calls for diffuse metamorphism and progressive deformation between the Backbone Range and the underlying metamorphic units.

4.3. Structural Domain III

Domain III is defined by S1 foliation striking NNW to NNE parallel to the belt, but contrary to domain I and II, S1 is dipping to the SE (Figure 4). S0 cannot be identified and the occurrence of a second foliation (S2)

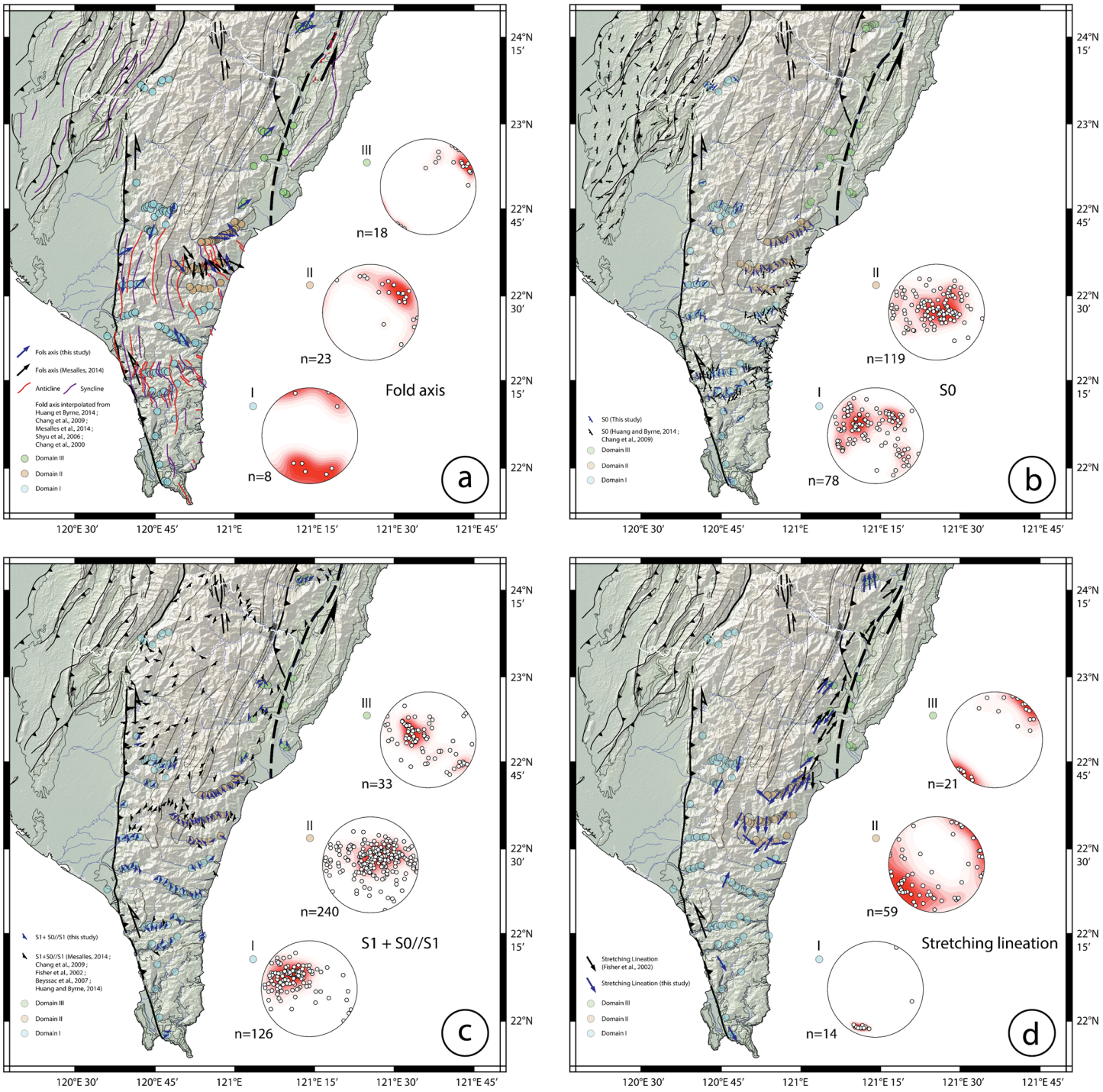

Figure 4. Maps of southern Taiwan with structural measurements from this study (blue symbols) and previous ones (black symbols). Stereograms from this study only, including (a) fold axes, (b) S_0 (bedding), (c) S_1 and $S_0//S_1$ (cleavages/schistosity), and (d) stretching lineations. See also the full compliation of structural measurements from our study in the Table A1.

altogether suggests that much higher deformation took place (Figure 10a). This domain corresponds to slates exposed in the eastern Backbone Range and schist of the Yuli Belt. Field observations were made along three narrow EW valleys (Luyeh, Yanping, and Chihpenchushan) where Eocene and Miocene slates are exposed (Figure 3). Stretching lineation L1 is shallowly plunging to NE parallel to S1 in agreement with orogen-parallel stretching. Such NE stretching direction is further kinematically consistent with late

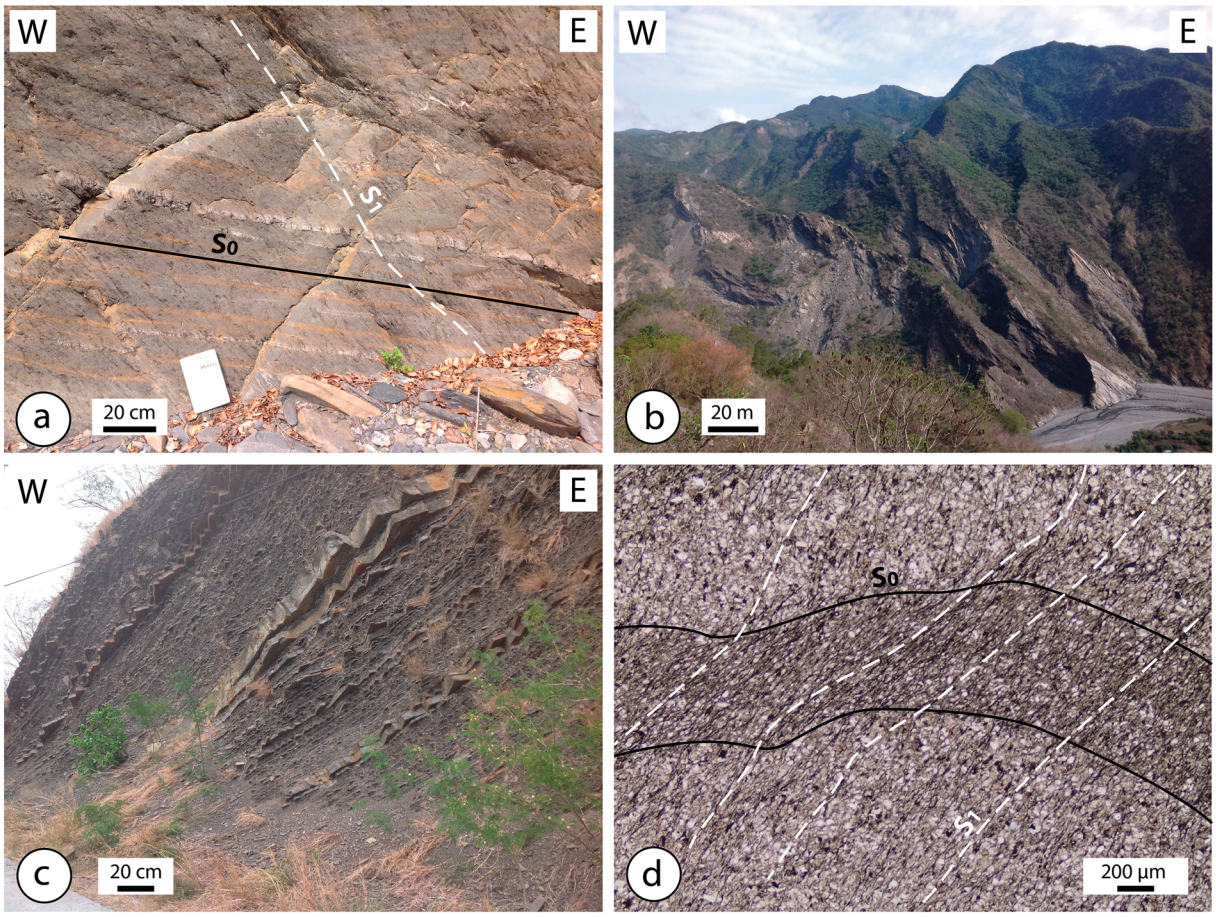

Figure 5. Examples of field structural features from the western BR of domain I. (a) Site 27 shows S_0, S_1 relationships in Miocene flysch series. (b) Site 29 showing the widespread and penetrative S_1 dipping to the east. (c) Site 13 showing bedding S_0 in unmetamorphosed Miocene turbidites. (d) Thin section from site 71 showing structural relationships between S_0 and S_1.

left-lateral shear that cuts across the main S1 foliation (Figure 10b). A small number of normal faults have been measured in the eastern Backbone Range (sites 226, 111) and all show consistent NNE-SSW extension (Figure 7). Like for domain II, brittle normal faulting is often found associated with Si-rich veins opening the foliation S1. This finding is consistent with the regional study of Fisher et al. (2002) who provided evidence of brittle normal faults indicating NS extension. To the north in the Zhuoxi Valley, structural data were acquired in metamorphic rocks near serpentinite blocks exposed within middle Miocene black schists typical of the hosted Yuli Belt rocks. There, S1 foliations are west dipping consistent with other data from the metamorphic basement (e.g., Fisher et al., 2002). Both stretching lineation L1 and brittle normal faulting (site 251) reflect a NNE extension parallel to the structural grain of the belt (Figures 4 and 7).

5. *P-T* Conditions in the Slate and Schist Belt: Backbone Range and Yuli Belt

5.1. RSCM Thermometry

We selected 43 samples for RSCM analyses from Eocene and Miocene slates of the Backbone Range of southern Taiwan (Figure 11a and Table 1). Our data complement previous RSCM data from the metamorphic basement collected along the southern cross-island highway (Beyssac et al., 2007).

To fill the gap with this transect, additional analyses have been performed in the eastern Backbone Range and in the Yuli Belt (Table 1).

RSCM results show an obvious NS gradient from <200 °C in the southern Hengchun Peninsula to almost 400 °C northward, at the latitude of 22°40′N. Consistently, the metamorphic basement northward shows

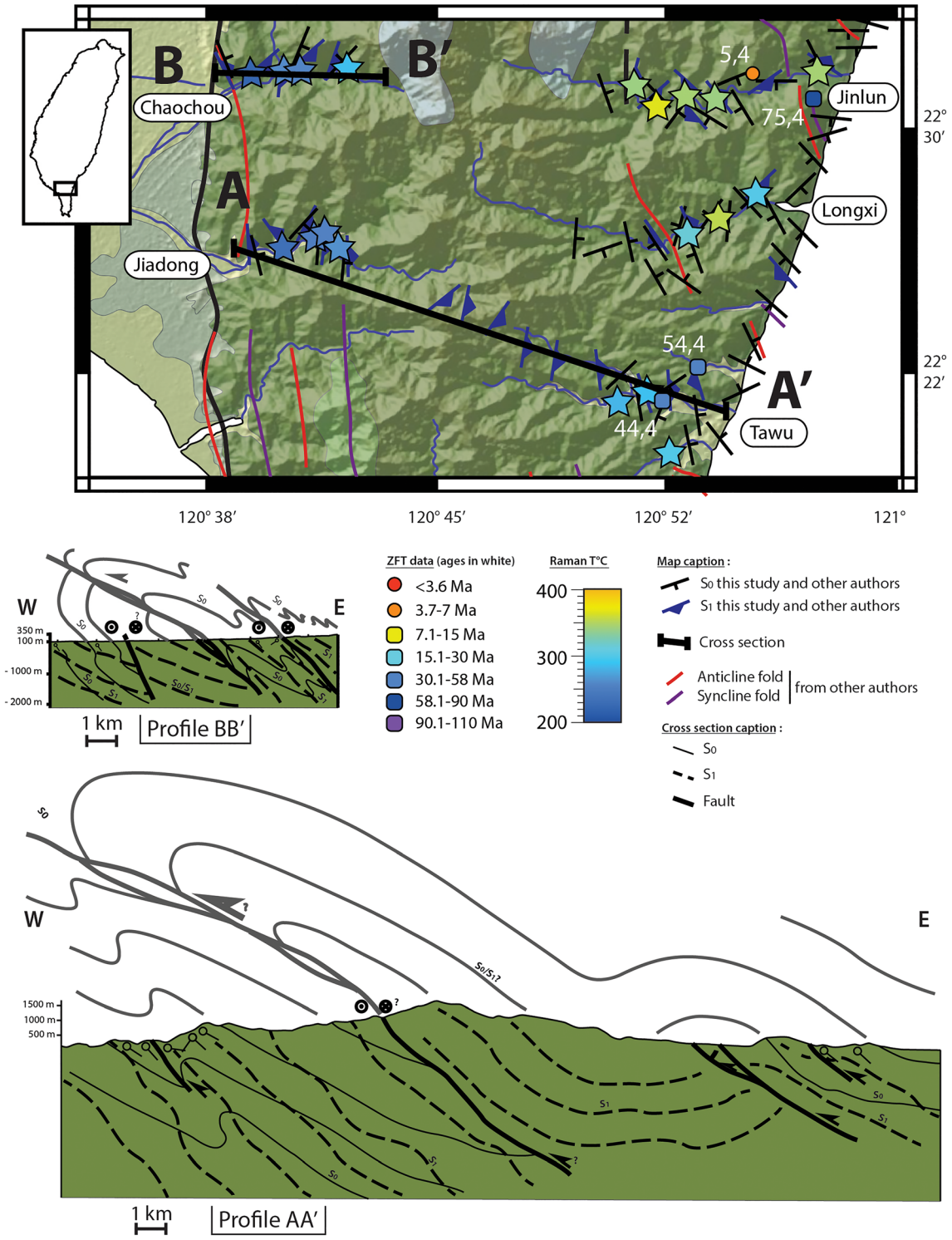

Figure 6. Structural map and cross sections in a region of structural domain I. S_1 is dipping mainly eastward and Miocene slates show west vergent folding. ZFT data are from previous low-temperature thermochronological studies (Lee et al., 2006; Liu et al., 2001; Mesalles et al., 2014; Willett et al., 2003). Other structural constraints on S_0 and S_1 are from Chang et al. (2009), Huang and Byrne (2014), Fisher et al. (2002), Mesalles et al. (2014), Chang et al. (2009), and Shyu et al. (2006).

higher temperatures of 550–350 °C. We note that intermediate temperatures of 320–400 °C are obtained from Eocene slates of the western BR. Another EW gradient is depicted by the range of temperatures obtained within the Miocene slates. Temperatures are indeed significantly lower at 200–320 °C in the

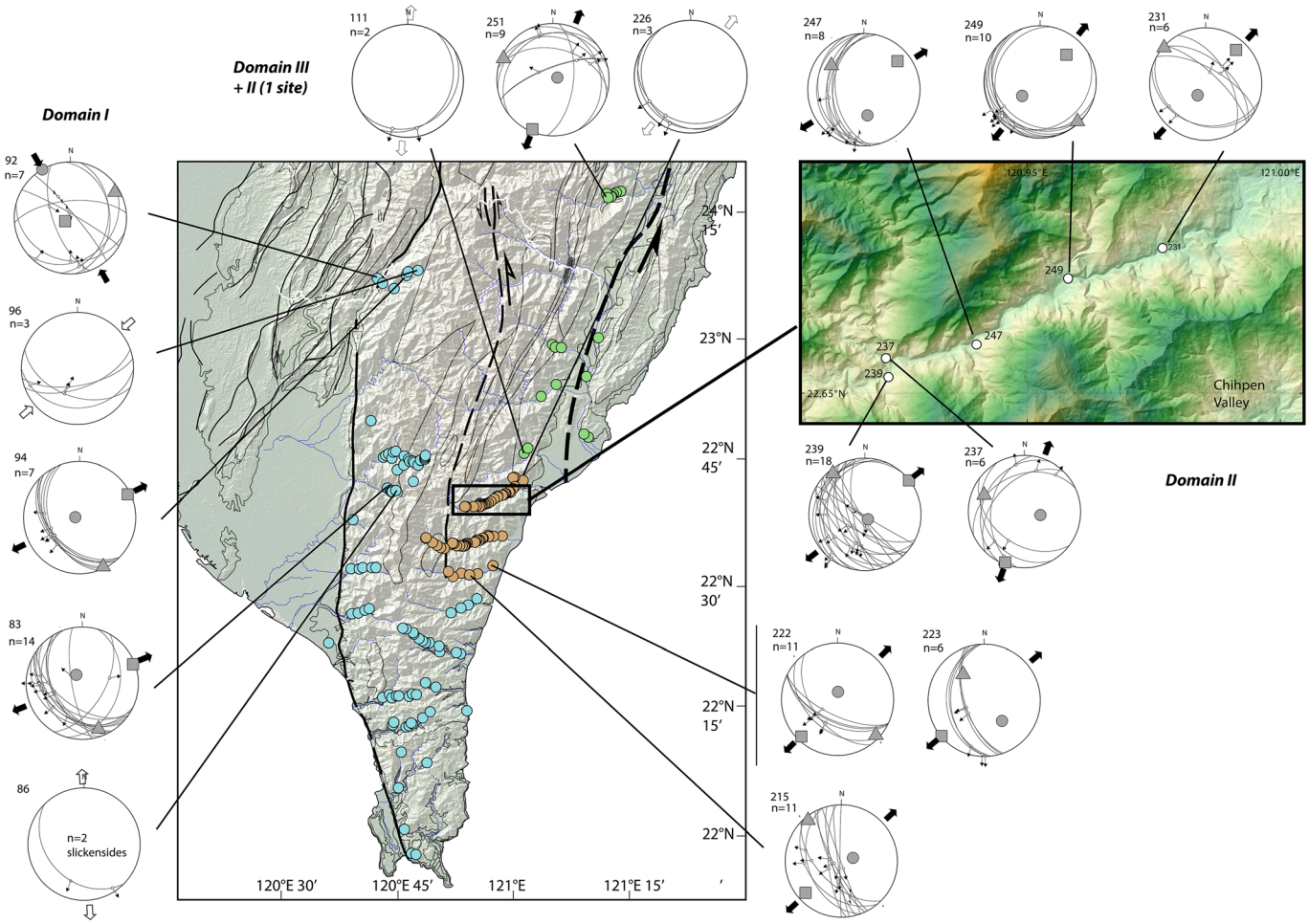

Figure 7. Results of fault slip analyses. Where inversion of slip have been performed, the given stress tensor is indicated by grey-filled circles (σ1), triangle (σ2), and square (σ3). We used Win_Tensor (Delvaux & Sperner, 2003) to plot and compute stress tensors based on formulation and inversion techniques from Angelier et al. (1990). For sites without sufficient fault slip data, white arrows depict a qualitative estimate of stress (σ3) direction.

structural domain I of western BR (Chaochou and Wutai Valleys) with respect to structural domain II where maximum temperatures are in the narrow 320–400 °C range (e.g., Taimali Valley). The increasing temperature trend therefore appears to correlate both with the older/deeper stratigraphic layers and the increasing ductile deformation in the eastern Central Range.

A comparison with the ages obtained from zircon fission-track analyses (Lee et al., 2006; Fuller et al., 2006; Mesalles et al., 2014) that have closure temperature of 240 ± 50 °C in the range of our RSCM estimates further allow defining whether these temperatures are preorogenic or synorogenic (Figures 11b and 12). The domain of reset zircon ages <7 Ma overlaps with the region where Miocene slates of the eastern BR show RSCM temperature of 320–400 °C (structural domain II). We infer that these temperatures were achieved during tectonic burial prior to exhumation and cooling during the latest Miocene. In the Wutai Valley, the unreset age zone overlaps with Eocene slates of that recorded equivalent RSCM temperatures of 320–400 °C. Because ZFT ages show precollision ages from 13 to 23 Ma (Lee et al., 2006; Mesalles et al., 2014), this region of the western BR did not record temperature above 300 °C during Taiwan collision (*t-T* diagrams are details in Figure A3). Therefore, the RSCM temperatures are interpreted to be preorogenic.

5.2. Pressure-Temperature Conditions Depicted From the Phengite-Chlorite Multiequilibrium Approach

Metapelite samples were selected for pressure-temperature estimates from postrift Miocene slates of the BR. Many minerals like phengite, chlorite, garnet, rutile, pyroxenes, and plagioclases inherited from Eurasian

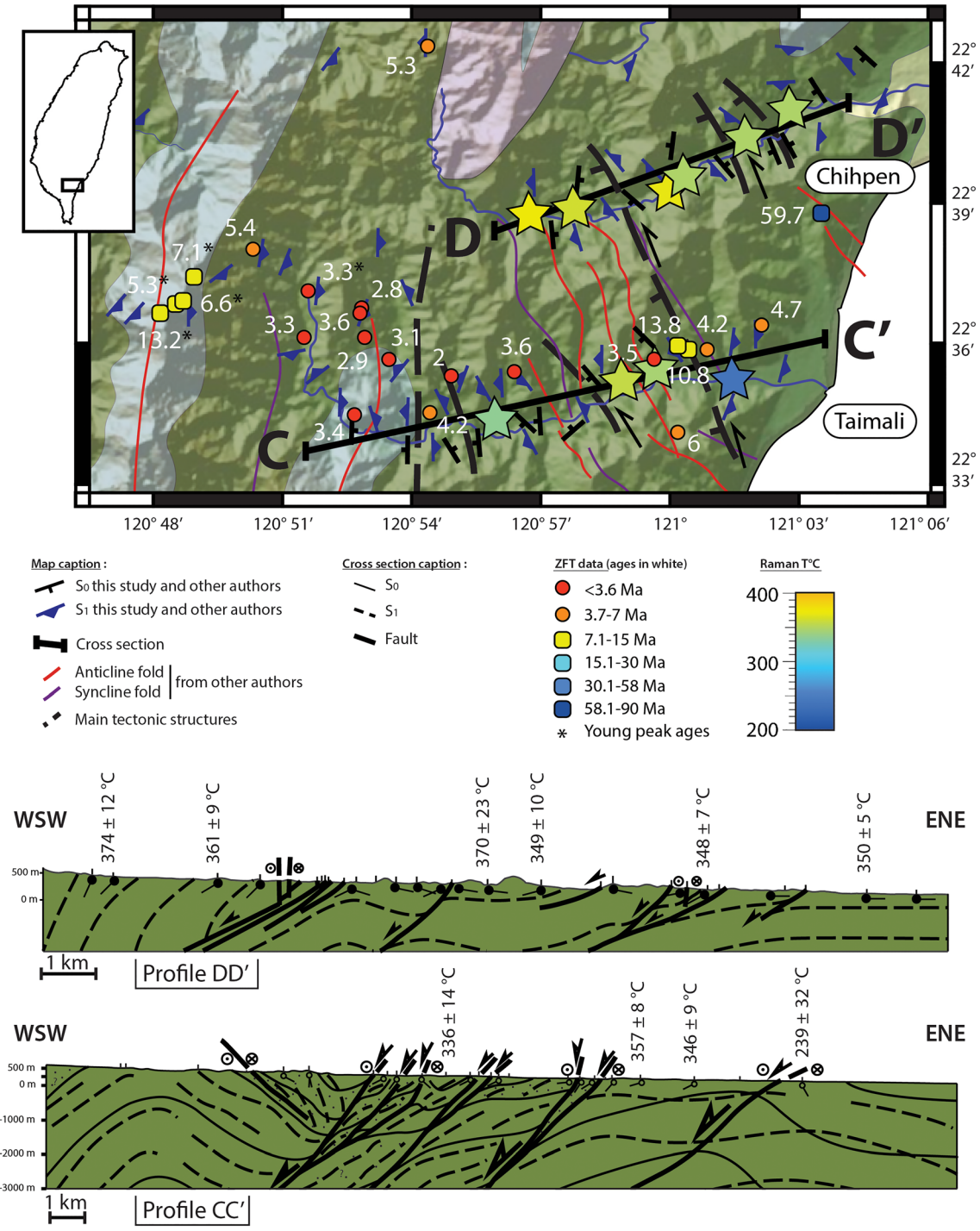

Figure 8. Structural map and cross sections in a region of structural domain II. This domain is defined by occurrence of SW dipping S_1 and well-defined N-S to NW-SE left-lateral normal faults; ZFT ages are from previous low-temperature thermochronological studies (Lee et al., 2006; Liu et al., 2001; Mesalles et al., 2014; Willett et al., 2003). Other structural constraints on S_0 and S_1 are from Chang et al. (2009), Huang and Byrne (2014), Fisher et al. (2002), Mesalles et al. (2014), Chang et al. (2000), and Shyu et al. (2006). We also show the temperatures obtained using RSCM analyses.

continent are not re-equilibrated during low-temperature metamorphism. Such inheritance imprints the whole rock analyses that make difficult the use of pseudosection. The local chemistry of equilibrated chlorite and phengites is therefore more efficient in defining pressure and temperature conditions. To avoid inheritance of mineral relics from the metamorphism that is recognized in Mesozoic and older

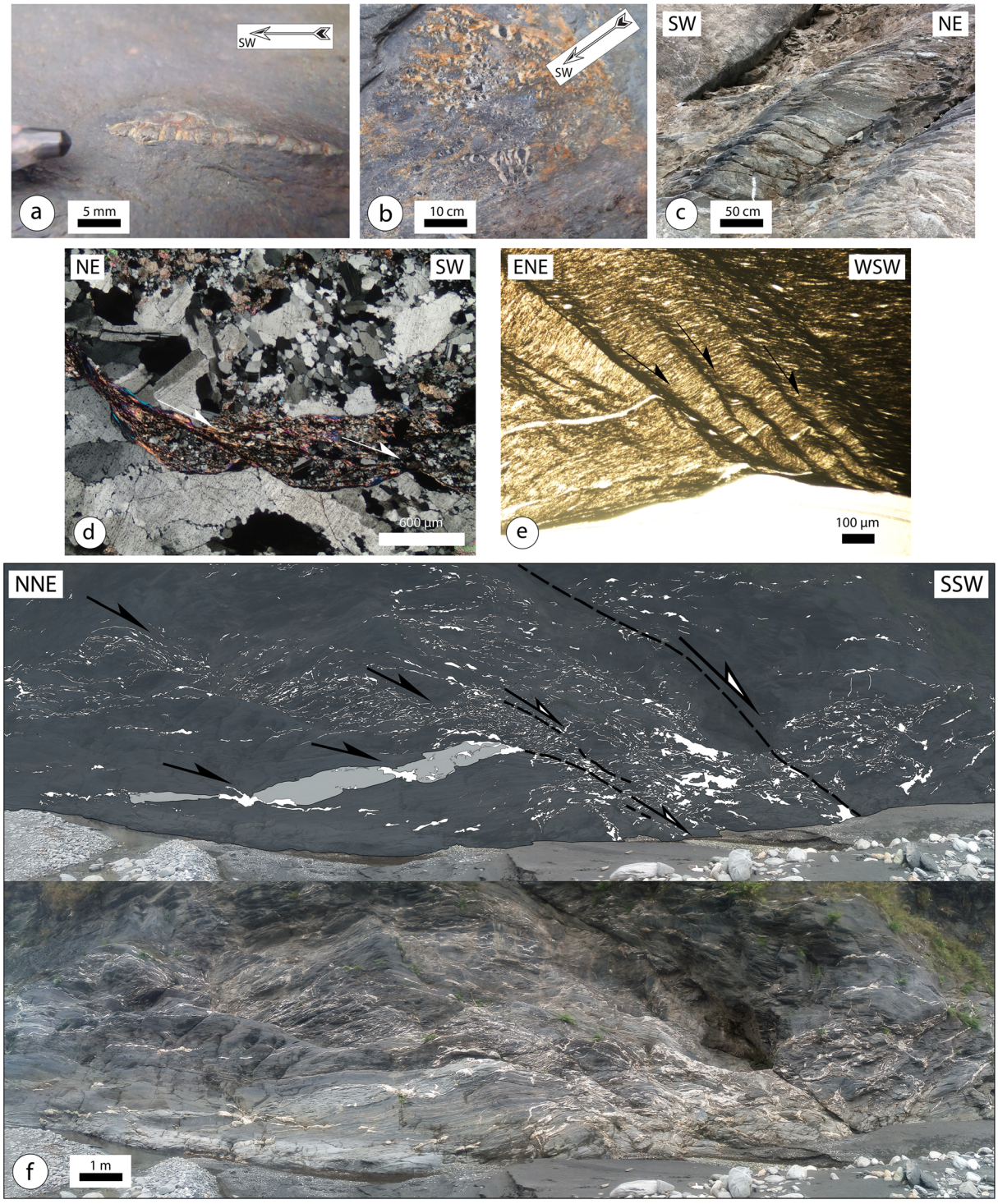

Figure 9. Field photographs and thin section of the eastern Backbone Range showing example of deformation patterns in domains II and III. (a) Site 231: stretching lineation in black schists defined by boudins of pyrite intercalated with precipitated quartz. (b) Site 117: stretching lineation defined by rounded clasts and pressure shadows of quartz in the stretching direction. (c) Site 223: simple shear deformed schists with normal top-to-the-SW kinematic. (d) Site 125: thin section showing a normal top-to-the-SW sense of shear band in which synkinematic chlorite and phengite minerals crystallized. (e) Site 134: S/C structure in flyschs with rotation of S_1 next to the shear bands and normal top-to-the-SW associate kinematics. (f) Site 111: deformed flyschs with asymmetric boudinage and left-lateral normal faults.

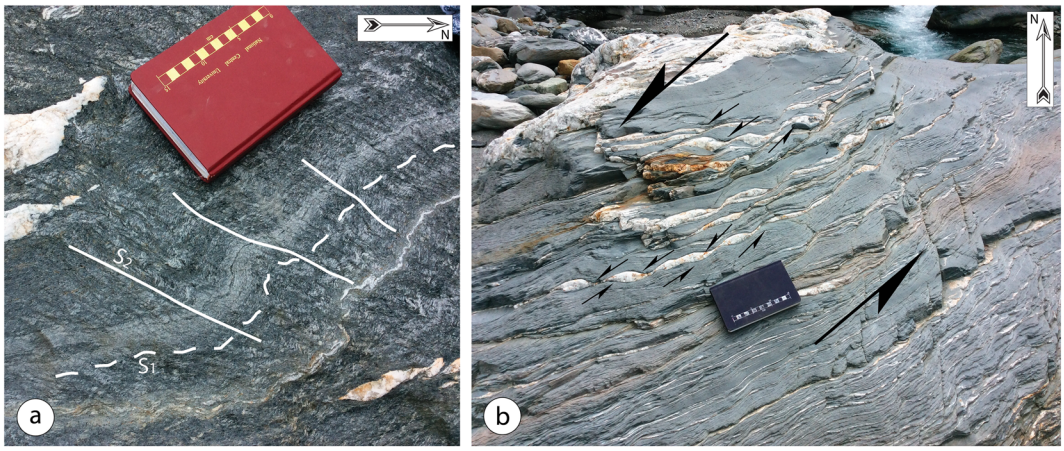

Figure 10. Field photographs of domain III as observed in the Backbone Range and the Yuli Belt. (a) Site 198: garnet schists of the Yuli belt with S_2 cutting across S_1. (b) Site 144: metasandstones with quartz veins boudinage and left-lateral kinematics.

rocks (Figure 2), measurements were conducted only on cogenetic phengite-chlorite pairs that crystalized parallel to the stretching lineation as shown on thin sections. The selected metapelites that did not present relevant phengite-chlorite equilibriums were rejected. In some samples inherited and synkinematic phengite grains can be distinguished in thin sections (e.g., 15–33; Figure A4); they are also characterized by different chemical compositions. The composition of synkinematic phengites fall closer to the muscovite pole (typically more than 60% of muscovite) than the inherited phengites in a celadonite-pyrophyllite-muscovite ternary diagram (Figures 13 and A4).

Results are presented from four metapelites (details in Table A2), representing chemical analyses on a total of 850 phengites and 282 chlorites of which 58 couples present equilibriums. Results of chemical analyses and PT estimates are detailed for sample CSC10 in Figure 13. This is a Miocene metapelite from the Yuli Belt sampled near the contact with the Chinshuishi ultramafic rocks (structural domain III) in which independent peak metamorphic *P-T* conditions of 15–17 kbar/530–550 °C (Keyser et al., 2016) have been estimated. CSC10 contains an assemblage of quartz + chlorite + phengite + garnet + epidote + feldspar + rutile + sphene. Figure 13 shows the classifications of phengites and chlorites (Figures 13a and 13b), the estimated range of equilibriums for the phengites using the method of Dubacq et al. (2010) (Figure 13c), and an example of equilibrium calculated for several pairs (Figure 13d) and for one pair at fixed *P* and *T* conditions to determine Gibbs free energy (dG; Figure 13e). Nonredundant equilibriums defined by the minimum of dG for each samples are presented in Figure 14.

Based on the phengite-chlorite-quartz-H_2O multiequilibrium calculation (Ganne et al., 2012) applied on CSC10 (46 mc-chl couples) we determine peak *P-T* conditions of 14–15 kbar and 350–400 °C (Figure 14). Phengite-chlorite pairs show a first exhumation stage from this metamorphic peak to *P-T* conditions of 4–7 kbar/325–410 °C. Exhumation in the shallow crust is recorded by final *P-T* conditions at 2–3 kbar and 330–350 °C. The peak PT conditions reached by the sample are in agreement with the RSCM temperature. The other samples 17-37 (2 mc-chl pairs), 17-39 (6 mc-chl pairs), and 17-40 (4 mc-chl pairs) are from Miocene slates of the Backbone Range that are representative of structural domain II of Chihben and Taimali Valleys (Figure 11a). They contain quartz + chlorite + phengite + calcite + feldspar ± rutile mineral assemblage. They all show consistent metamorphic peak conditions at 2–8 kbar and 330–400 °C in agreement with the measured RSCM temperature at 374 ± 12 °C, 350 ± 5 °C, and 357 ± 8 °C, for 17-37, 17-39, and 17-40, respectively. Sample 17-40 presents a pair at 2 kbar and 270 °C. *P* and *T* paths inferred from the different phengite-chlorite equilibriums show exhumation along a near-isothermal gradient to *P-T* conditions of 2–3 kbar and 330–350 °C.

To provide peak metamorphic conditions, the phengite-chlorite multiequilibrium approach allows resolving progressive exhumation in the middle-to-upper crust from 5–6 kbar (15–20 km) to 2–3 kbar (10–6 km) that represent the last stages of deformation observed in domain II. We also note that the final PT conditions compatible with phengite-chlorite crystallization at 2–3 kbar can be compared with closure temperature

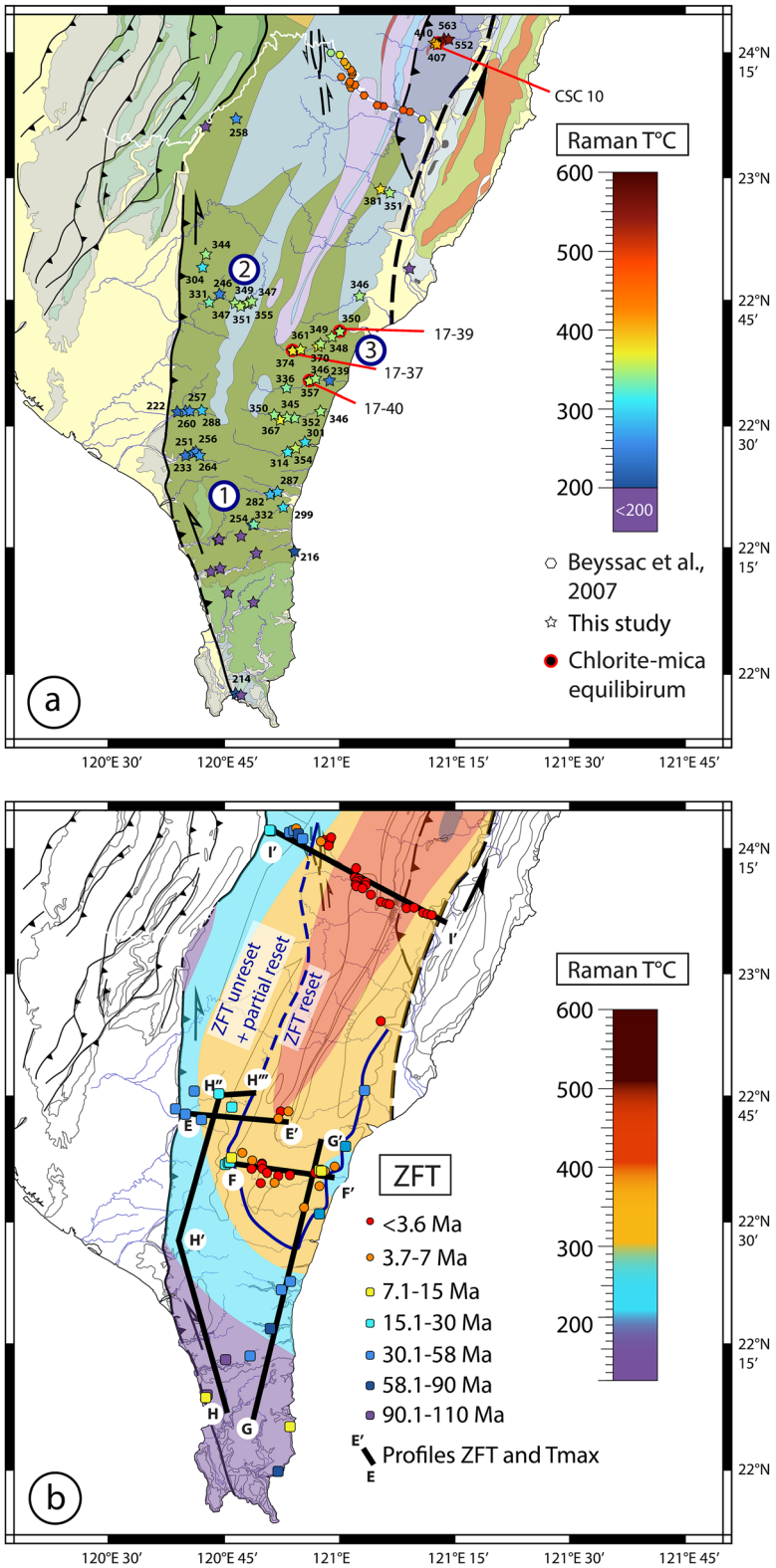

Figure 11. (a) Individual RSCM temperature distribution in southern Taiwan. Red circles show samples where the chlorite-phengite equilibrium approach has been applied. Areas labeled 1, 2, and 3 are used in Figure A3 showing a comparison between maximum temperature and low-temperature thermochronological dates. (b) Contours of RSCM temperatures. Zircon fission-track ages (ZFT) are after Lee et al. (2006), Liu et al. (2001), Mesalles et al. (2014), and Willett et al. (2003). The blue line depicts the limit between reset syncollision ages (<7 Ma) and unreset or partially reset samples. Thick black lines (E-E′, F-F′, G-G′, H-H′, I-I′) represent profiles shown in Figure 12 onto which both RSCM and ZFT ages are plotted.

Table 1
Results of RSCM Temperature Analyses

Locality	Samples	Latitude	Longitude	Unit	T_{max} (°C)	Standard deviation	1σ	Nb spectrum
4	15-01	22.16342	120.75322	Backbone	<200			19
5	15-02	22.14299	120.80757	Backbone	<200			20
6	15-03	22.24373	120.81446	Backbone	<200			23
7	15-05	22.2078	120.71725	Backbone	<200			17
8	15-06	22.21239	120.73626	Backbone	<200			18
9	15-07	22.21239	120.73626	Backbone	<200			17
11	15-08	22.27058	120.73568	Backbone	<200			17
12	15-09	22.27039	120.73232	Backbone	<200			18
14	15-11	22.44625	120.68596	Backbone	256	11.65	2.82	17
15	15-12	22.44551	120.67982	Backbone	251	18.86	4.44	18
17	15-13	22.43932	120.66354	Backbone	233	7.51	2.26	11
21	15-14	22.5277	120.64364	Backbone	222	11.69	2.68	19
22	15-15	22.52847	120.6631	Backbone	260	10.52	2.48	18
	15-16	22.52873	120.67112	Backbone	257	38.95	8.93	19
26	15-17	22.53038	120.69808	Backbone	288	9.07	2.34	15
30	15-18	22.7463	120.76726	Backbone	347	5.05	1.13	20
35	15-19	22.74063	120.77968	Backbone	351	12.31	2.75	20
40	15-20	22.75116	120.80365	Backbone	347	5.52	1.30	18
43	15-21	22.7465	120.79541	Backbone	349	5.86	1.38	18
47	15-22	22.84434	120.70699	Backbone	344	8.30	1.95	18
	15-23	22.81825	120.69879	Backbone	304	32.91	8.49	15
	15-24	22.43952	120.69286	Backbone	264	27.45	6.29	19
60	15-25	22.27779	120.77977	Backbone	<200			23
69	15-26	22.3363	120.86999	Backbone	299	8.90	2.22	16
70	15-27	22.36636	120.85815	Backbone	287	9.86	2.73	13
71	15-28	22.36169	120.84397	Backbone	282	23.28	5.48	18
73	15-29	22.30006	120.80325	Backbone	254	16.27	4.34	14
74	15-30A	22.30003	120.80537	Backbone	332	25.27	6.12	17
74	15-30B	22.30003	120.80537	Backbone	251	14.53	3.52	17
77	15-31	22.24646	120.89451	Backbone	216	19.860	4.96	16
80	15-32	22.76336	120.73545	Backbone	246	8.50	2.06	17
82	15-33	22.74912	120.71374	Backbone	331	12.99	3.06	18
	16-04a	22.81594	121.13974	LM	<200			11
83	17-01B	22.68488	120.30940	Backbone	301	13.94	4.02	12
91	17-04	23.10390	120.70225	WF	<200			20
95	17-08A	23.11784	120.76684	Backbone	258	10.11	2.20	21
98	17-11A	21.96036	120.77475	KM	214	17.58	4.26	17
99	17-13B	21.95785	120.78509	KM	<200			15
100	17-14B	22.59423	120.96948	Backbone	239	31.88	14.25	5
102	17-16	22.59511	120.93890	Backbone	346	8.48	2.00	18
112	17-25	22.96744	121.09803	Backbone	351	5.84	1.62	13
112	17-25B	22.96744	121.09803	Backbone	355	9.83	2.72	13
113	17-26	22.74398	120.79334	Backbone	355	8.63	2.09	17
116	17-29	22.76639	121.02493	Backbone	346	6.79	1.60	18
118	17-31	22.67808	120.97560	Backbone	348	7.16	1.98	13
120	17-32	22.66773	120.95172	Backbone	349	10.02	2.50	16
121	17-33	22.66289	120.94468	Backbone	370	22.95	5.00	21
125	17-37	22.65153	120.89147	Backbone	374	11.53	3.08	14
126	17-38	22.65238	120.90779	Backbone	361	8.71	2.32	14
127	17-39	22.68817	120.99222	Backbone	350	4.87	1.25	15
128	17-40	22.58960	120.92715	Backbone	357	7.84	1.96	16
131	17-43	22.57539	120.87688	Backbone	336	14.33	3.37	18
133	17-44A	22.51489	120.89546	Backbone	352	5.10	1.31	15
134	17-45B	22.51766	120.87902	Backbone	345	5.47	1.29	18
135	17-46B	22.51252	120.86395	Backbone	367	17.08	4.56	14
136	17-47	22.52268	120.85254	Backbone	350	6.95	1.79	15
137	17-48	22.44960	120.88013	Backbone	314	22.90	5.55	17
139	17-50	22.45805	120.89676	Backbone	354	4.53	2.26	4
140	17-51	22.46718	120.91625	Backbone	301	21.43	5.72	14
141	17-52	22.53307	120.95009	Backbone	346	6.40	1.39	21

Table 1
(continued)

Locality	Samples	Latitude	Longitude	Unit	T_{max} (°C)	Standard deviation	1σ	Nb spectrum
144	17-55A	22.97412	121.07759	Backbone	381	9.06	2.34	15
144	17-55B	22.97412	121.07759	Backbone	397	15.61	3.90	16
196	CSC4	23.26832	121.19695	Yuli	407	16.29	3.95	17
198	CSC10	23.26961	121.19377	Yuli	410	13.73	3.43	16
202	CSC12	23.27608	121.21550	Yuli	563	16.70	4.17	16
203	CSC13B	23.27612	121.22364	Yuli	552	30.36	7.59	16

Note. Temperature below 200 °C are not constrained precisely and therefore do not present standard deviation and 1σ. 1σ = Standard deviation $\frac{2}{\sqrt{nb\ speectrums}}$.
KM = Kenting mélange, LM = Lichi mélange, WF = Western Foothills.

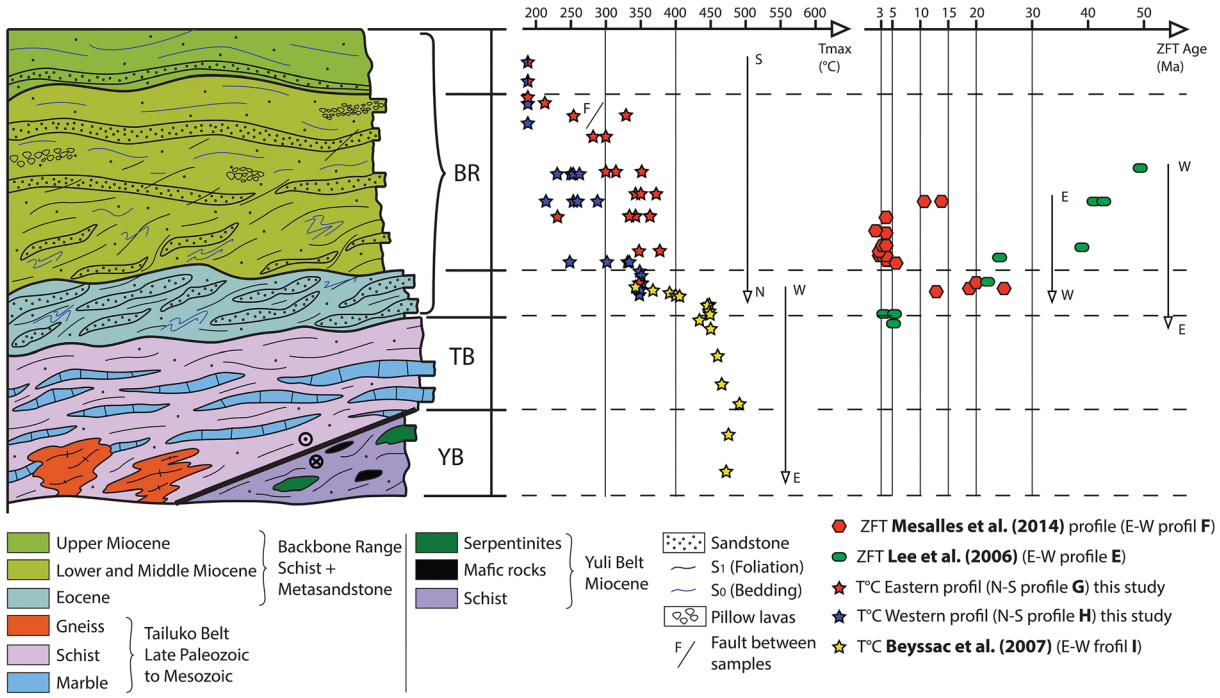

Figure 12. RSCM temperatures positioned according to the preorogenic stratigraphy of central Taiwan. On the right, RSCM constraints from our study are shown as blue and red stars and those from Beyssac et al. (2007) as yellow stars. Low-temperature thermochronological dates are from Mesalles et al. (2014) (red hexagons) and Lee et al. (2006) (green circles). All the different symbols correspond to RSCM temperatures and ZFT age constraints extracted from profiles E-E′, F-F′, G-G′, H-H′, and I-I′, which are located in Figure 11b.

of ZFT. Because domain II shows ZFT ages with cooling ages of approximately 7–5 Ma (Mesalles et al., 2014) our results confirm that Miocene slates were at 10–6 km approximately 7–5 Ma ago, thus placing important constraints on the exhumation paths in the eastern BR.

6. Discussion

6.1. Crustal-Scale Geology: Inherited Versus Syncollisional Thermal History

Southern Taiwan offers the opportunity to investigate the thermal structure of an orogen a few million years after collision inception at 7–6 Ma and subaerial erosion started approximately 3 Ma. Thermochronological data (Mesalles et al., 2014), morphological observations (Giletycz et al., 2015), and moderate RSCM temperatures altogether indicate very recent exhumation of the uppermost Miocene sedimentary cover.

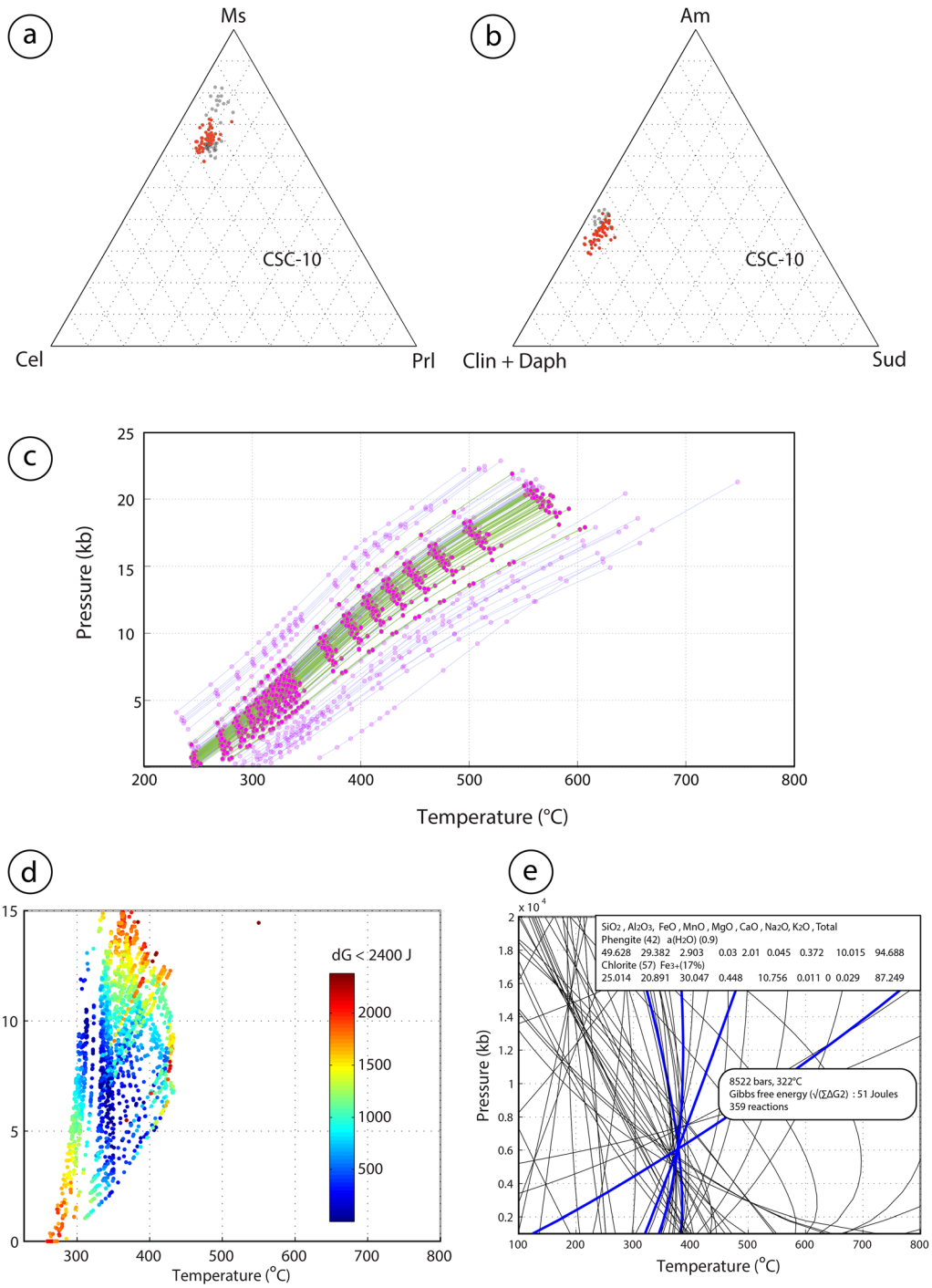

Figure 13. Chlorite-phengite approach and results shown for sample CSC10 as an example. The same method was used for the other samples (17-37, 17-39, 17-40; see also Figure 11a for location). Ternary plots of the phyllosilicate compositions from the sample CSC10 in (a) celadonite-muscovite-pyrophyllite (phengite; 107 analyses) and (b) amesite-(clinochlore + daphnite)-sudoite (chlorite; 64 analyses) end-member. The grey dots correspond to the chlorite/phengite compositions obtained from conventional spot analysis (microprobe). The red dots correspond to the chlorite/phengite compositions in equilibrium (46 points). The analyses were first filtered before multiequilibrium calculation on the basis of the compositional criteria detailed in Vidal and Parra (2000). (c) Pressure and temperature equilibrium conditions using the phengite-quartz-H_2O multiequilibrium calculation (Dubacq et al., 2010). Each blue line is one phengite, differently hydrated at each (mauve) point (aH_2O 0.1 to 0.99). Each green line superimposed on the graph is one phengite equilibrated with one chlorite using the phengite-chlorite-quartz-H_2O multiequilibrium calculation (Ganne et al., 2012). (d) Chlorite/phengite pairs (46; see Table A2) analyzed within sample CSC10 using the phengite-chlorite-quartz-H_2O multiequilibrium calculation (Ganne et al., 2012). Chlorite and phengite have been contoured for the sum of the Gibbs free energy $\sum\Delta G2$ of seven independent reactions (see explanations in the text). Sum is <2,400 J. (e) Example of chlorite/phengite pair (20) analyzed within sample CSC10. Mineral compositions used for PT calculations are listed on the right top side of the grids.

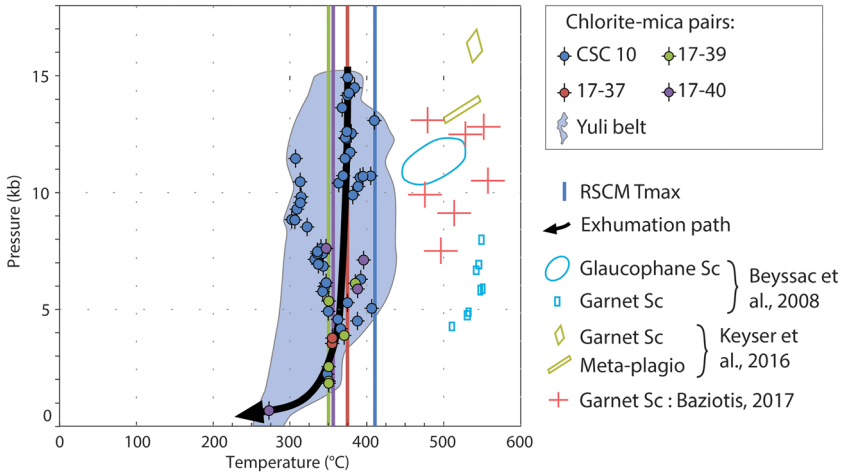

Figure 14. Pressure-temperature estimates and paths determined from chlorite-phengite multiequilibriums. For 17-37, 17-39, and 17-40, points present nonredundant data with a precision of ±10 °C and ±800 bars. Results from CSC10 (Yuli Belt) are shown (see also Figure 13). A selection of other PT estimates from the Yuli Belt in the north (Beyssac et al., 2008) and in the same region (Keyser et al., 2016) is also shown.

Figure 15 shows a crustal-scale section across southern Taiwan at the latitude of Taimali Valley. The section summarizes the main brittle-ductile tectonic features observed in the field, how they root at depth, and how these features are related to peak RSCM paleo-temperatures. First, the organization of maximum temperatures displays an antiformal structure mimicking the large-scale folding that characterizes southern Taiwan. This pattern of RSCM temperatures has also been noticed by other RSCM constraints along the southern cross-island highway (Beyssac et al., 2007). The western sector accounts for the abrupt transition between predominantly brittle deformation of unmetamorphosed sedimentary rocks of the western foreland thrust belt with the slate belt of the Backbone Range (Brown et al., 2012; Mouthereau et al., 2001, 2002; Tang et al., 2011; Wiltschko et al., 2010; Huang & Byrne, 2014).

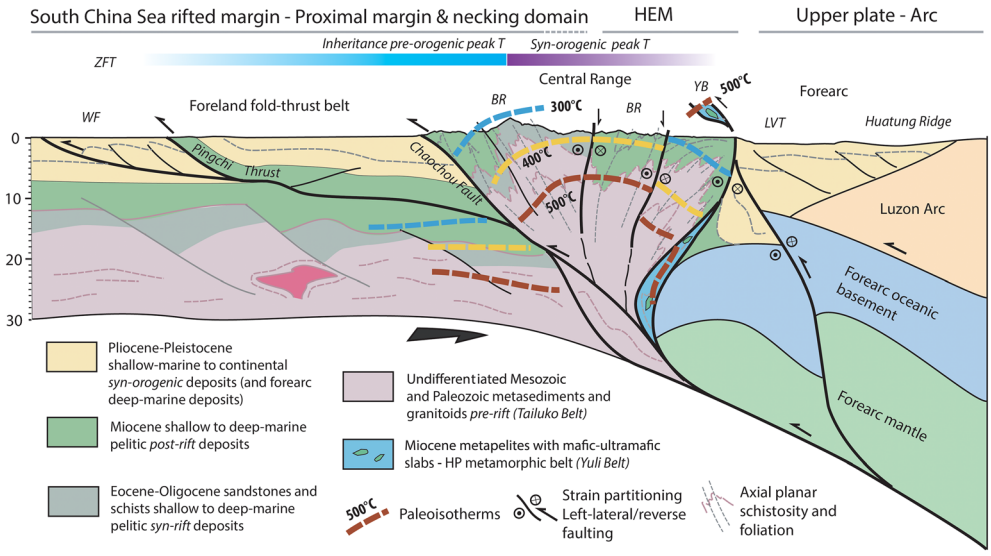

Figure 15. Crustal cross section of southern Taiwan at the latitude of Taimali. Contours of peak RSCM temperatures have been interpolated based on the spatial distribution shown in Figure 11 for the Central Range (Backbone Range and Yuli Belt). The RSCM temperatures in the foreland are deduced from the current thermal gradients (see text). We also added information on the probable position of the different rifted margin units from the proximal unthinned domain, to the necking zone and hyperextended margin (HEM). HP units are interpreted to have been exhumed along a left-lateral shear zone. CSC10 sample from which PT conditions have been determined is located to the north, so YB is out of the plane of the section.

In the hanging wall of the Chaochou Fault and its southern extension, the Hengchun Fault, bounding the Kenting mélange, the westward dip of RSCM-defined paleo-isotherms follows the western flank of the fold outlined by the Eocene-Miocene boundary. These peak temperatures, although considered precollisional, do not seem to be affected by the contractional, shorter-wavelength, outcrop-scale to mesoscale folding/cleavage features. This finding supports the small component of localized shear and orthogonal shortening in the western BR (domain I) as seen in the field and in thin sections.

In addition, the spatial distribution of partially reset and fully reset ages also well outlines the antiform of the Central Range (Figure 11a). The mapping of RSCM paleo-isotherms (Figure 11b) indicates that they are cut by the N-S-to-N20°E striking Chaochou-Hengchun Fault system. Such obliquity emphasizes that the Chaochou-Hengchun Fault system is a more recent, out-of-sequence, tectonic feature. This result is further supported by the generally younger (<3 Ma) synorogenic apatite fission-track ages in the vicinity of the Chaochou Fault (Lock, 2007; Simoes et al., 2012). In order to provide a maximum estimate of the thermal jump across the Chaochou Fault we have positioned the 300 °C, 400 °C, and 500 °C isotherms in the footwall of the Chaochou Fault inferred using the present-day thermal gradient of about 40 °C/km in the foreland (Chi & Reed, 2008). From these constraints we derive an apparent vertical structural offset of 10 km. Such a large displacement is consistent with the interpretation that the fault is a high-angle east dipping and deep-seated inherited fault accommodating uplift of Central Range relative to the subsiding Pingtung basin (e.g., Mouthereau et al., 2001, 2002; Camanni et al., 2016). A Chaochou basement fault hypothesis is further supported by the Jiashian earthquake ($M > 6$) that nucleated at 20 km in the eastern Western Foothills of southern Taiwan (Huang et al., 2013), well below the shallow detachment surface.

Also consistent with the regional antiformal architecture, paleo-isotherms are east dipping in eastern BR. They further cut at high angle the mesoscale folds. We have shown (see section 5.1) that temperatures measured in domain II are synorogenic; therefore, to explain the cross-cutting relationships between RSCM temperatures and folds, the noncoaxial strain and cleavages must have occurred close to the thermal peak. There is also an apparent important jump in RSCM temperature across the normal left-lateral shear zones defined in the east of the section in the Taimali Valley (Figure 15). A eastward decrease of 100 °C across this domain is also coincident with a change from steeply dipping to shallow dipping cleavages in slates and evidence for EW trending folds parallel to the coast (see also Figures 4 and 11b). We interpret that this pattern reflects the juxtaposition of the lower grade rocks exposed southern Taiwan with the higher-grade rocks of the eastern Backbone Range, thus defining a left-lateral shear zone along the coast.

The antiformal organization of RSCM temperature of southern Central Range is the result of large-scale folding across a wide zone of left-lateral shearing. Late thrusting in the western BR explains preservation of precollisional peak temperature acquired in the SCS rifted margin while longer-term strike-slip shearing, synorogenic burial, and exhumation occurred in the eastern BR. These inferences suggest that the thermal pattern reconstructed across the Taiwan mountain belt, characterized by higher metamorphic grade toward the east, do not simply reflect the long-term, east directed, continuous subduction, accretion, and thickening of the continental crust.

6.2. Exhumation Paths, Tectonic Burial in Southern Taiwan, and Inversion of the SCS Rifted Margin

PT conditions from metapelites show that the eastern BR (domain II) and YB (domain III) recorded, after deposition at 15–11 Ma (see also Figure 2), contrasted prograde histories to depths between 46–50 km (14–15 kbar) for YB and 15–20 km (5–6 kbar) for BR (Figure 16). All previous PT paths from the Yuli Belt, including those from the same outcrop (Keyser et al., 2016), yielded PT conditions characterized by higher temperatures but similar pressures (Figure 16). Considering that we obtain similar temperatures from two independent approaches relying on individual minerals in the bulk rock (e.g., Raman spectrometry and Chl-Phg multiequilibrium), we are confident that our schist samples did not reach temperatures above 400 °C. The differences of temperatures (>100 °C) observed with previous estimates (Figure 16) indicate the coexistence of inherited/detrital mineral phases with synexhumation chlorite and phengite. The whole rock chemistry is therefore not in thermodynamic equilibrium, thus precluding the use of the pseudosection method as was classically done.

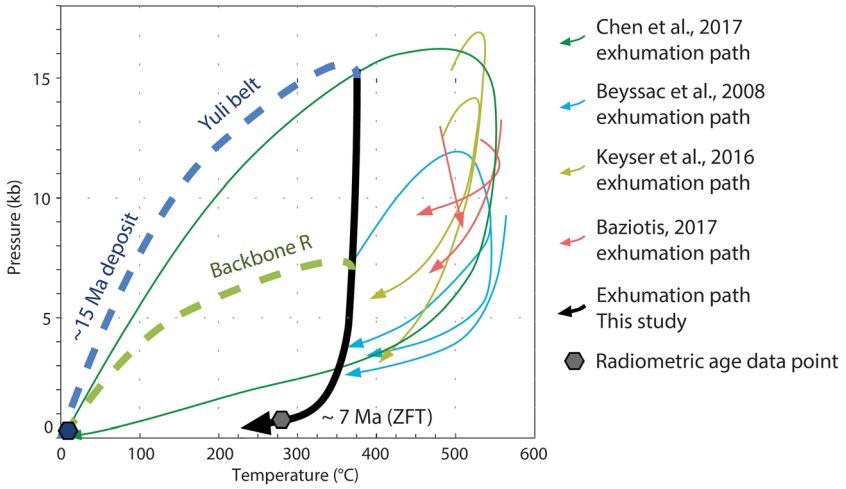

Figure 16. PT paths for the Yuli Belt and Backbone Range deduced from Chl-Phg multiequilibriums. For comparison we also show exhumation paths proposed by other authors (Baziotis et al., 2017; Beyssac et al., 2008; Chen et al., 2017; Keyser et al., 2016).

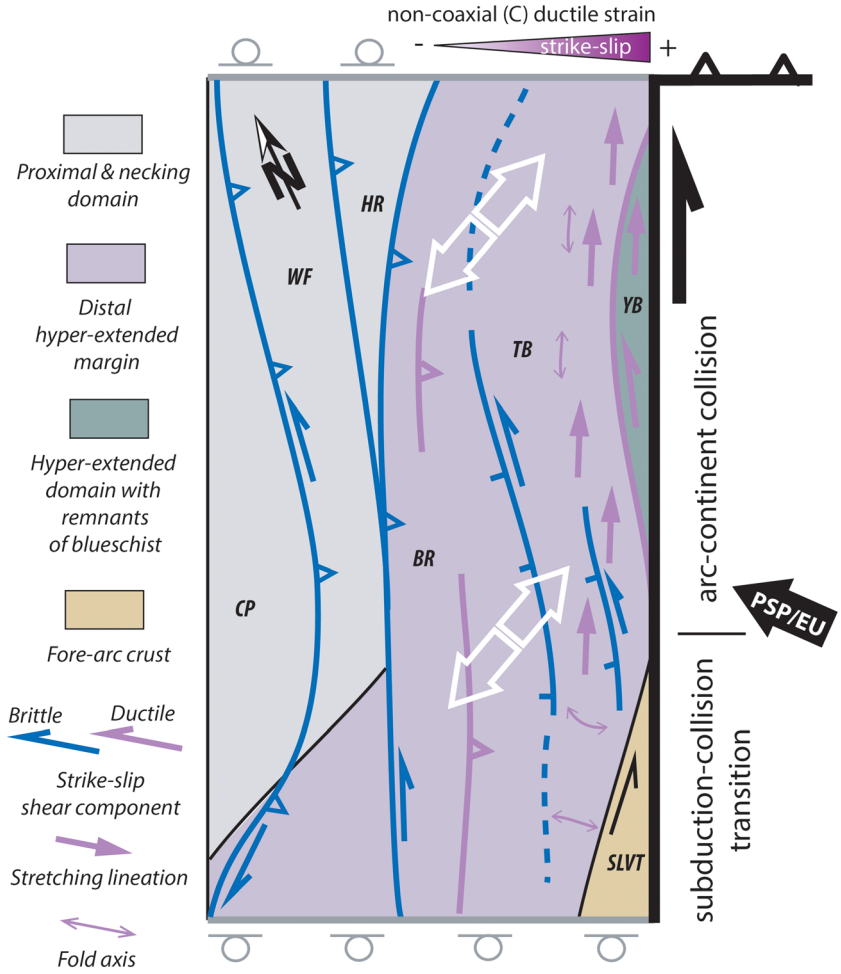

Figure 17. Synthetic sketch summarizing strain partitioning in Taiwan as discrete (brittle, partitioned) and diffuse (ductile, nonpartitioned) contraction, extension, and transcurrent motions. SCS rifted margin architecture is shown to have played a key role during orogeny. CP = Coastal Plain, WF = Western Foothills, HR = Hsuehshan Range, BR = Backbone Range, TB = Tailuko Belt, YB = Yuli Belt, SLVT = South Longitudinal Valley Trough. Grey thick lines depict domains where free slip and escape tectonics may occur.

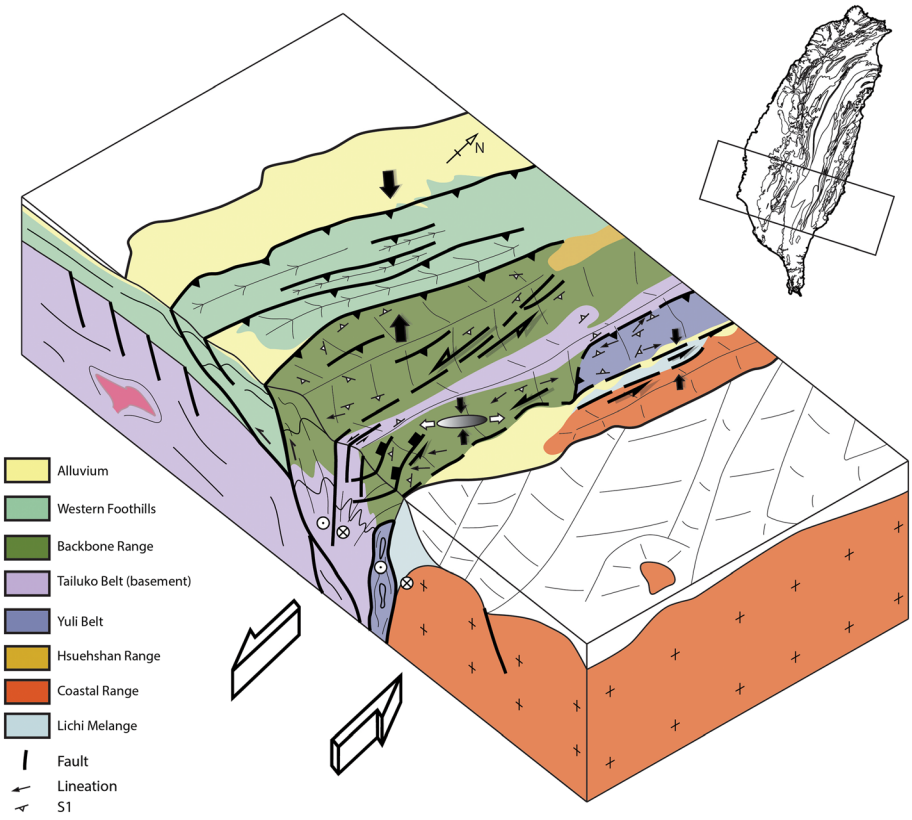

Figure 18. The 3-D bloc diagram showing kinematics and strain distribution of transpression in the Taiwan arc-continent collision of southern Taiwan. Exhumation of HP rocks results from transcurrent motion in eastern Taiwan along the suture zone that reflect shearing of hyperextended margin or OCT. Contraction localizes in the western BR while brittle transtension in the Central Range. Strain ellipsoid represents deformation in a diffuse transpressional domain.

Figure 15 shows that HP rocks of the Miocene YB resulted from the burial of the most distal part of the SCS distal rifted margin or oceanic crust. Exhumation of the YB is interpreted to have occurred along a major left-lateral shear zone associated with deformation of the forearc crust and collision with the Luzon Arc. Both YB and BR were then exhumed as a coherent unit along the same path from depths of 6–10 km (2–3 kbar) and temperature of 350 °C (Figure 16). Taking into account the thermal history defined by ZFT data in the region (Mesalles et al., 2014) we know that slates of the eastern BR recorded onset of accretion at around 7–5 Ma. ZFT-based thermal modeling further argues for increased subaerial erosion from 3 Ma, in accordance with depositional unconformity in the foreland and age of forearc consumption (Mesalles et al., 2014). To quantify how much tectonic burial is needed to reproduce our peak metamorphic conditions, we need to constrain the original sediment overburden since the deposition Miocene strata (15–11 Ma) to Pliocene (3 Ma; Mesalles et al., 2014) when sediments became first eroded. In the west Taiwan basin, the thickness of mid-Miocene-to-Pliocene sediments range from 1 to nearly 4 km, locally in some extensional rift basin (Tainan basin; e.g., Tensi et al., 2006). After Teng et al. (1991), 2 km of Miocene sediments are exposed in the Hsuehshan Range, but the overlying mid-late Miocene and lower Pliocene strata have been removed by erosion. The same authors estimated in the western Backbone Range a minimum of 1 km for the middle Miocene. Based on these constraints we consider 2 km of mid-Miocene as a reasonable average estimate for the total thickness of mid-Miocene to Pliocene in the distal part of SCS margin in Taiwan area. We infer that domain II recorded maximum tectonic burial equivalent to 4–8 km. This represents the original thickness of the tectonic overburden on the eastern side of the orogen. Since 3 Ma, published (Mesalles et al., 2014) subaerial exhumation rates show consistent total erosion of 5 km. These results together with structure and kinematics shown in Figure 15 indicate that the missing tectonic overburden likely corresponds to the eroded part of the overthrusting YB, which was exhumed laterally along the strike-slip shear zone at the front of the forearc crust (Figure 15). Because the YB and the BR are characterized by the same original "flysch-type" middle Miocene deposits, and that southern Central Range of Taiwan (Hengchun

Peninsula) is interpreted as an inverted distal rifted margin, we suggest that they were originally both part of the hyperextended SCS rifted margin (see section 2.3). Indeed, recent seismic refraction and reflection data further revealed that the crust offshore southern Taiwan and below Hengchun Peninsula is transitional (McIntosh et al., 2013). The YB experienced subduction to 50 km and HP metamorphism in the south in a domain probably similar to the current Hengchun Peninsula. But its later exhumation and contact with eastern BR units in the latest Miocene occurred to the north, in the mature collision zone.

6.3. Long-Term/Short-Term Strain Partitioning, Plate Kinematics, and Role of Rift Architecture

Figures 17 and 18 aim at summarizing the main three-dimensional kinematic patterns obtained in this study. First, collision obliquity induces strain partitioning between contraction orthogonal to the plate boundary and left-lateral shearing parallel to the plate boundary. Orthogonal shortening is recorded in the western BR and in the Western Foothills (domain I). This domain coincides with deformation of the proximal and necking domain of the SCS rifted margin characterized by the deposition of synrift Eocene-Oligocene sediments (Western Foothills, Hsuehshan Range, and possibly part of the western BR). This structural domain is in contact with the hyperextended crust of the SCS margin (eastern BR, YB, and TB) of domain II where those deposits are lacking (see also section 2.3). The western Central Range therefore places two domains with different initial crustal thicknesses, 30 km in the west to typically 10 km or below according to geophysical survey off southern Taiwan (Lester et al., 2013), in the east, over a very short distance. The transition is sharp and striking N-S, oblique to the main structural grain of N70°E that characterizes the SCS margin. It has been suggested that the narrow boundary in the west is a former north striking transform zone, which has inherited the NS direction of spreading and extension on the SCS extension in the middle Miocene (12–16 Ma; Angelier et al., 1990; Taylor & Hayes, 1980; Pautot et al., 1986; Briais et al., 1993). The inversion of the transform fault may explain the synchronous exhumation pattern along-strike (Byrne et al., 2011; Lee et al., 2015).

The strike-slip component is accommodated by increasing localization of ductile left-lateral shear in domain III, a characteristic also recognized northward in the Tananao Schist (Pulver et al., 2002). This ductile strain pattern is overprinted by brittle transtensional deformation in domain II (Figure 17).

This kinematics is further generally consistent with left-lateral strike-slip faulting along the active Longitudinal Valley Fault (e.g., Lee et al., 1998; Shyu et al., 2005; Shyu et al., 2006, 2008), extending probably offshore in the South Longitudinal Valley Trough (LVT of Figure 17) and the Huatung Ridge, which connects northward with the Lichi mélange. Therefore, exhumation of HP rocks in the Yuli Belt from about 50 km, left-lateral ductile shearing in the Central Range, strike-slip faulting in the Longitudinal Valley Fault and collision suturing appear closely kinematically related (Figure 18).

We infer that exhumation of HP metamorphic units of eastern Taiwan occurred soon after 16–11 Ma ago (depositional age of middle Miocene sediments) in association with the north directed transport of subducted series below the forearc crust. Existing plate reconstructions account for the north directed motion of the Philippine Sea Plate at about 15 Ma oblique to the plate boundary (e.g., Wu et al., 2016). The recent change in PSP/EU motion from north directed to WNW directed motions that defined the current plate kinematics occurred between 7 and 3 Ma. This change was responsible for westward migration of deformation and partitioning of the oblique left-lateral component long the Chaochou Fault and Hengchun Fault (e.g., Shyu et al., 2005; Giletycz et al., 2017), accompanied by lateral extrusion of the Pingtung plain (Lacombe et al., 2001; Lin et al., 2010; Ching et al., 2007).

Present-day extension slightly oblique to the orogen direction prevails in the Central Range (e.g., Lin et al., 2010; Mouthereau et al., 2009). In our study, this extension is reflected in the field by a WSW-ENE to SSW-NNE extension associated with north striking left-lateral normal fault zones (Figure 15). Consistent with distributed deformation at oblique convergent margin, extension is expected to occur simultaneously with contraction and transcurrent motion (e.g., Teyssier et al., 1995). This extension may further be enhanced by the gravitational stresses arising from the combination of topographic difference along the axis of the main chain and subduction zones bounding the Central Range to the north and the south. We infer that Taiwan represents a striking example where oblique collision was accommodated in a wide left-lateral shear domain and was later partitioned into a strike-slip component parallel to the suture zone and contraction orthogonal to the belt.

6.4. Transcurrent Deformation and Two-Dimensional Numerical Modeling

Published thermal, kinematic, and mechanical models of Taiwan (e.g., Barr & Dahlen, 1990; Simoes et al., 2007; Yamato et al., 2009) have successfully reproduced the distribution of metamorphic grades, temperatures, and thermochronological ages assuming two-dimensional tectonic wedge models. One category of models assumes that plate convergence is accommodated by underplating that occurs as discrete windows of ductile duplexes to reproduce fast exhumation in central Taiwan. They imply that Taiwan is a thin-skinned orogenic wedge shaped by west directed allochthonous and low-grade metamorphic rocks, translated above aseismic ductile duplexes of higher-grade metamorphic rocks (Malavieille & Trullenque, 2009; Simoes et al., 2007). Alternative interpretations suggest that deformation occurs by the differential thickening of upper and lower crust, in a thick-skinned manner (e.g., Yamato et al., 2009). In the first hypothesis, inherited features such as samples showing anomalously low RSCM temperature or preorogenic thermochronological ages are preserved only in structurally higher allochthonous units that escaped subduction, whereas in the second hypothesis they are preserved in originally shallower and younger units where total exhumation is the lowest.

Based on our study, we show a lack of large thrusting in the western BR (and to some extent in the eastern BR of Hengchun Peninsula), a domain also characterized by preorogenic ZFT ages and shortening orthogonal to the strike of the belt (Figure 15). These observations rather in support of the second structural model of Taiwan. However, this view has received much less attention because it fails to reproduce the west directed nappe stacking and low-angle thrusting required by present-day N110° rapid plate convergence and shortening of presumably thin-skinned Taiwan orogenic wedge. Here we show that transcurrent ductile deformation dominated the long-term strain pattern in Taiwan, required by the motion of the Philippine Sea Plate relative to Eurasia since 15 Ma. Although plate kinematics changed to less obliquity in the past 5–3 Myr, we suggest that present-day strain partitioning is ongoing as reflected by the coexistence of brittle left-lateral shear, active oblique extension, and contraction (Byrne et al., 2011; Shyu et al., 2005; Mouthereau et al., 2009).

7. Conclusion

Our aim was to investigate the strain distribution and peak metamorphism in southern Taiwan where collision is presumably the most recent. We presented new field-based constraints on the structure of southern Taiwan, combined with new RSCM temperatures as well as new estimates of pressure-temperature conditions in low- and high-grade metamorphic units in the Central Range of Taiwan (Backbone Range and Yuli Belt) using a chlorite-phengite multiequilibrium approach. Altogether these new data allow us to propose a consistent model of strain partitioning across Taiwan, from orthogonal contraction in the west, transtension, and left-lateral shear in the east, active possibly since 15 Ma and associated with the north directed motion of the Philippine Sea Plate. We emphasize that nappe stacking is absent in the western Backbone Range and thermal structure is inherited from the Paleogene rift evolution. We argue that convergence across Taiwan was accommodated by orthogonal shortening in large-scale crustal folding and penetrative cleavages, and by north directed transport along a large initially ductile shear zone in the east, interpreted as the reactivation of a former north directed paleo-transform margin. This kinematic framework is suggested to be responsible for burial to 20–50 km and exhumation of rocks in the Backbone Range and Yuli Belt to about 10 km between 15 and 7 Ma. With the subsequent arc-continent collision at about 3 Ma, the decrease in obliquity of the plate convergence was responsible for out-of-sequence thrusting in the western Taiwan (Chaochou Fault), left-lateral normal faulting in the Central Range, and left-lateral thrusting along the Longitudinal Valley Fault. These results, including lateral motion within the accretionary wedge, must be taken into account in tectonic models of the Taiwan collision.

Acknowledgments
The authors acknowledge the financial support by LIA CNRS-MOST D3E and the ANR-Carnot ISIFOR. We greatly appreciated the assistance of Chin-ho Tsai, Garry Chuang, Antoine Poujol, Prabodha Das, Johnny Li, Dominikus Deka Dewangga, Chih-Ying Yeh, Wen-Han Lo, and Pika Liu during the fieldwork. We are grateful to Yoann Denèle for the discussion on transtensional deformation. Philippe De Parseval at the Raymond Castaing Center greatly helps for microprobe analyses and interpretations. We finally warmly acknowledge the reviewers, for their constructive comments and efforts. All data presented in this article are shared and made freely available on the open-access repository Zenodo (doi: 10.5281/zenodo.3629859).

References

Angelier, J. (1990). Inversion of field data in fault tectonics to obtain the regional stress—III. A new rapid direct inversion method by analytical means. *Geophysical Journal International*, *103*, 363–376. https://doi.org/10.1111/j.1365-246X.1990.tb01777.x

Angelier, J., Bergerat, F., Hao-Tsu, C., & Teh-Quei, L. (1990). Tectonic analysis and the evolution of a curved collision belt: The Hsuehshan Range, Northern Taiwan. *Tectonophysics*, *183*(1–4), 77–96. https://doi.org/10.1016/0040-1951(90)90189-F

Barckhausen, U., Engels, M., Franke, D., Ladage, S., & Pubellier, M. (2014). Evolution of the South China Sea: Revised ages for breakup and seafloor spreading. *Marine and Petroleum Geology*, *58*, 599–611. https://doi.org/10.1016/j.marpetgeo.2014.02.022

Barr, D., Dahlen, F. A., & Mcpham, D. C. (1991). Brittle Frictional Mountain Building 3. Low-grade metamorphism. *Journal of Geophysical Research*, *96*(B6), 10,319–10,338.

Barr, T. D., & Dahlen, F. A. (1989). Brittle frictional mountain builiding, 2. Thermal structure and heat budget. *Journal of Geophysical Research*, *94*, 3923–3947.

Barr, T. D., & Dahlen, F. A. (1990). Constraints on friction and stress in the Taiwan fold-and-thrust belt from heat flow and geochronology. *Geology*, *18*, 111–115.

Barrier, E., Huchon, P., & Aurelio, M. (1991). Philippine fault: A key for Philippine kinematics. *Geology*, *19*(1), 32. https://doi.org/10.1130/0091-7613(1991)019<0032:PFAKFP>2.3.CO;2

Baziotis, I., Tsai, C., Ernst, W. G., Jahn, B., & Iizuka, Y. (2017). New *P–T* constraints on the Tamayen glaucophane-bearing rocks, eastern Taiwan: Perple _ X modelling results and geodynamic implications. *Journal of Metamorphic Geology*, *35*, 35–54. https://doi.org/10.1111/jmg.12218

Beyssac, O., Goffé, B., Chopin, C., & Rouzaud, J. N. (2002). Raman spectra of carbonaceous material in metasediments: A new geothermometer. *Journal of Metamorphic Geology*, *20*(9), 859–871. https://doi.org/10.1046/j.1525-1314.2002.00408.x

Beyssac, O., Negro, F., Simoes, M., Chan, Y. C., & Chen, Y. G. (2008). High-pressure metamorphism in Taiwan: From oceanic subduction to arc-continent collision? *Terra Nova*, *20*(2), 118–125. https://doi.org/10.1111/j.1365-3121.2008.00796.x

Beyssac, O., Simoes, M., Avouac, J. P., Farley, K. A., Chen, Y., Chan, Y., & Goffé, B. (2007). Late Cenozoic metamorphic evolution and exhumation of Taiwan. *Tectonics*, *26*, TC6001. https://doi.org/10.1029/2006TC002064

Briais, A., Patriat, P., & Tapponnier, P. (1993). Updated interpretation of magnetic anomalies and seafloor spreading stages in the South China Sea: Implications for the Tertiary tectonics of Southeast Asia. *Journal of Geophysical Research*, *98*(B4), 6299–6328. https://doi.org/10.1029/92JB02280

Brown, D., Alvarez-Marron, J., Schimmel, M., Wu, Y.-M., & Camanni, G. (2012). The structure and kinematics of the central Taiwan mountain belt derived from geological and seismicity data. *Tectonics*, *31*, TC5013. https://doi.org/10.1029/2012TC003156

Byrne, T., Chan, Y.-C., Rau, R.-J., Lu, C.-Y., Lee, Y.-H., & Wang, Y.-J. (2011). *The arc–continent collision in Taiwan. In Frontiers in Earth Sciences*, (Vol. 4, pp. 213–245). Berlin, Heidelberg: Springer. https://doi.org/10.1007/978-3-540-88558-0_8

Camanni, G., Alvarez-Marron, J., Brown, D., Ayala, C., Wu, Y.-M., & Hsieh, H.-H. (2016). The deep structure of south-central Taiwan illuminated by seismic tomography and earthquake hypocenter data. *Tectonophysics*, *679*, 235–245. https://doi.org/10.1016/j.tecto.2015.09.016

Chang, C., Angelier, J., & Lu, C. (2009). Polyphase deformation in a newly emerged accretionary prism: Folding, faulting and rotation in the southern Taiwan mountain range. *Tectonophysics*, *466*(3–4), 395–408. https://doi.org/10.1016/j.tecto.2007.11.002

Chang, C. P., Angelier, J., & Huang, C. Y. (2000). Origin and evolution of a melange: The active plate boundary and suture zone of the Longitudinal Valley, Taiwan. *Tectonophysics*, *325*(1–2), 43–62. https://doi.org/10.1016/S0040-1951(00)00130-X

Chang, C. P., Angelier, J., Huang, C. Y., & Liu, C. S. (2001). Structural evolution and significance of a mélange in a collision belt: the Lichi mélange and the Taiwan arc–continent collision. *Geological Magazine*, *138*(6), 633–651. https://doi.org/10.1017/S0016756801005970

Chen, C.-H., Chu, H. T., Liou, J. G., & Ernst, W. G. (1983). Explanatory notes for the metamorphic facies map of Taiwan. *Special Publication of the Central Geological Survey*, *2*, 1–32.

Chen, C. T., Chan, Y. C., Lu, C. Y., Simoes, M., & Beyssac, O. (2011). Nappe structure revealed by thermal constraints in the Taiwan metamorphic belt. *Terra Nova*, *23*(2), 85–91. https://doi.org/10.1111/j.1365-3121.2011.00987.x

Chen, W., Chung, S., Chou, H., Zugeerbai, Z., Shao, W., & Lee, Y.-H. (2017). A reinterpretation of the metamorphic Yuli belt: Evidence for a middle-late Miocene accretionary prism in eastern Taiwan. *Tectonics*, *36*, 188–206. https://doi.org/10.1002/2016TC004383

Chi, W. C., & Reed, D. L. (2008). Evolution of shallow, crustal thermal structure from subduction to collision: An example from Taiwan. *Bulletin of the Geological Society of America*, *120*(5–6), 679–690. https://doi.org/10.1130/B26210.1

Ching, K. E., Rau, R. J., Lee, J. C., & Hu, J. C. (2007). Contemporary deformation of tectonic escape in SW Taiwan from GPS observations, 1995–2005. *Earth and Planetary Science Letters*, *262*(3–4), 601–619. https://doi.org/10.1016/j.epsl.2007.08.017

Chung, S., & Sun, S. (1992). A new genetic model for the East Taiwan Ophiolite and its implications for Dupal domains in the Northern Hemisphere. *Earth and Planetary Science Letters*, *109*, 133–145.

Clark, M. B., Fisher, D. M., Lu, C.-Y., & Chen, C. (1993). Kinematic analyses of the Hsuehshan range, Taiwan: A large-scale pop-up structure. *Tectonics*, *12*(1), 205–217.

Clift, P. D., Lin, A. T. S., Carter, A., Wu, F., Draut, A. E., Lai, T. H., et al. (2008). Post-collisional collapse in the wake of migrating arc-continent collision in the Ilan Basin, Taiwan. In A. E. Draut, P. D. Clift, & D. W. Scholl (Eds.), *Formation and Applications of the Sedimentary Record in Arc Collision Zones. The Geological Society of America: Special Paper 436* (Vol. 436, pp. 257–278). https://doi.org/10.1130/2008.2436(12)

Crespi, J. M., Chan, Y. C., & Swaim, M. S. (1996). Synorogenic extension and exhumation of the Taiwan hinterland. *Geology*, *24*(3), 247–250. https://doi.org/10.1130/0091-7613(1996)024<0247:SEAEOT>2.3.CO;2

Dadson, S. J., Hovius, N., Chen, H., Dade, W. B., Hsieh, M. L., Willett, S. D., et al. (2003). Links between erosion, runoff variability and seismicity in the Taiwan orogen. *Nature*, *426*(6967), 648–651. https://doi.org/10.1038/nature02150

Dahlen, F. A. (1990). Critical taper model of fold-and-thrust belts and accretionary wedges. *Annual Review of Earth and Planetary Sciences*, *18*, 55–99.

Davis, D., Dahlen, F. A., & Suppe, J. (1983). Mechanics of fold-and-thrust belts and accretionary wedges: Cohesive Coulomb theory. *Journal of Geophysical Research*, *88*(B2), 1153–1172. https://doi.org/10.1029/JB089iB12p10087

Delchini, S., Lahfid, A., Plunder, A., & Michard, A. (2016). Applicability of the RSCM geothermometry approach in a complex tectono-metamorphic context: The Jebilet massif case study (Variscan Belt, Morocco). *Lithos*, *256–257*, 1–12. https://doi.org/10.1016/j.lithos.2016.04.007

Delvaux, D., & Sperner, B. (2003). New aspects of tectonic stress inversion with reference to the TENSOR program. *Geological Society, London, Special Publications*, *212*, 75–100. https://doi.org/10.1144/GSL.SP.2003.212.01.06

Dubacq, B., Vidal, O., & de Andrade, V. (2010). Dehydration of dioctahedral aluminous phyllosilicates: Thermodynamic modelling and implications for thermobarometric estimates. *Contributions to Mineralogy and Petrology*, *159*(2), 159–174. https://doi.org/10.1007/s00410-009-0421-6

Eakin, D. H., Mcintosh, K. D., Van Avendonk, H. J. A., Lavier, L., Lester, R., Liu, C., & Lee, C. (2014). Crustal-scale seismic profiles across the Manila subduction zone: The transition from intraoceanic subduction to incipient collision. *Journal of Geophysical Research: Solid Earth*, *119*, 1–17. https://doi.org/10.1002/2013JB010395

Fisher, D. M., Lu, C.-Y., & Chu, H.-T. (2002). Taiwan slate belt: Insights into the ductile interior of an arc-continent collision. *Geological Society of America: Special Paper*, *358*, 93–106. https://doi.org/10.1130/0-8137-2358-2.93

Franke, D. (2013). Rifting, lithosphere breakup and volcanism: Comparison of magma-poor and volcanic rifted margins. *Marine and Petroleum Geology*, *43*, 63–87. https://doi.org/10.1016/j.marpetgeo.2012.11.003

Franke, D., Savva, D., Pubellier, M., Steuer, S., Mouly, B., Auxietre, J. L., et al. (2014). The final rifting evolution in the South China Sea. *Marine and Petroleum Geology*, *58*, 704–720. https://doi.org/10.1016/j.marpetgeo.2013.11.020

Fuller, C., Willett, S. D., Fischer, D., & Lu, C. Y. (2006). A thermomechanical wedge model of Taiwan constrained by fission-track thermochronometry. *Tectonophysics*, *425*, 1–24. https://doi.org/10.1016/j.tecto.2006.05.018

Ganne, J., de Andrade, V., Weinberg, R. F., Vidal, O., Dubacq, B., Kagambega, N., et al. (2012). Modern-style plate subduction preserved in the Palaeoproterozoic West African craton. *Nature Geoscience*, *5*(1), 60–65. https://doi.org/10.1038/ngeo1321

Giletycz, S., Loget, N., Chang, C., & Mouthereau, F. (2015). Geomorphology transient fluvial landscape and preservation of low-relief terrains in an emerging orogen: Example from Hengchun Peninsula, Taiwan. *Geomorphology*, *231*, 169–181. https://doi.org/10.1016/j.geomorph.2014.11.026

Giletycz, S. J., Chang, C. P., Lin, A. T. S., Ching, K. E., & Shyu, J. B. H. (2017). Improved alignment of the Hengchun Fault (southern Taiwan) based on fieldwork, structure-from-motion, shallow drilling, and levelling data. *Tectonophysics*, *721*, 435–447. https://doi.org/10.1016/j.tecto.2017.10.018

Gozzard, S., Kusznir, N., Franke, D., Cullen, A., Reemst, P., & Henstra, G. (2019). South China Sea crustal thickness and oceanic lithosphere distribution from satellite gravity inversion. *Petroleum Geoscience*, *25*(1), 112–128. https://doi.org/10.1144/petgeo2016-162

Ho, C. S. (1986). A synthesis of the geologic evolution of Taiwan. *Tectonophysics*, *125*(1–3), 1–16. https://doi.org/10.1016/0040-1951(86)90004-1

Hovius, N., Stark, C. P., Hao-Tsu, C., & Jiun-Chuan, L. (2000). Supply and removal of sediment in a landslide-dominated mountain belt: Central Range, Taiwan. *The Journal of Geology*, *108*(1), 73–89. https://doi.org/10.1086/314387

Hsu, W.-H., Byrne, T. B., Ouimet, W., Lee, Y.-H., Chen, Y.-G., van Soest, M., & Hodges, K. (2016). Pleistocene onset of rapid, punctuated exhumation in the eastern Central Range of the Taiwan orogenic belt. *Geology*, *44*(9), 719–722. https://doi.org/10.1130/G37914.1

Huang, C., & Byrne, T. B. (2014). Tectonic evolution of an active tectonostratigraphic boundary in accretionary wedge: An example from the Tulungwan-Chaochou Fault system, southern Taiwan. *Journal of Structural Geology*, *69*, 320–333. https://doi.org/10.1016/j.jsg.2014.06.007

Huang, C.-Y., Chang, C.-H., Yao, B., & Chang, C.-P. (2008). The Lichi mélange: A collision mélange formation along early arcward backthrusts during forearc basin closure, Taiwan arc-continent collision. *The Geological Society of America Special Paper*, *436*.

Huang, C.-Y., Chen, W. H., Wang, M. H., Lin, C. T., Yang, S., Li, X., et al. (2018). Earth-Science Reviews Juxtaposed sequence stratigraphy, temporal-spatial variations of sedimentation and development of modern-forming forearc Lichi mélange in North Luzon Trough forearc basin onshore and offshore eastern Taiwan: An overview. *Earth-Science Reviews*, *182*(March 2017), 102–140. https://doi.org/10.1016/j.earscirev.2018.01.015

Huang, C.-Y., Yuan, P. B., & Tsao, S.-J. (2006). Temporal and spatial records of active arc-continent collision in Taiwan: A synthesis. *Geological Society of America Bulletin*, *118*(3–4), 274–288. https://doi.org/10.1130/B25527.1

Huang, M.-H., Dreger, D., Bürgmann, R., Yoo, S.-H., & Hashimoto, M. (2013). Joint inversion of seismic and geodetic data for the source of the 2010 March 4, M_w 6.3 Jia-Shian, SW Taiwan, earthquake. *Geophysical Journal International*, *193*, 1608–1626.

Huang, T. C., Chen, M. P., & Chi, W. R. (1979). Calcareous nannofossils from the red shale of the ophiolite-mélange complex, eastern Taiwan. *Memoir of the Geological Society of China*, *3*, 131–138.

Jahn, B. (1986). Mid-ocean ridge or marginal basin origin of the East Taiwan ophiolite: Chemical and isotopic evidence. *Contributions to Mineralogy and Petrology*, *92*, 194–206.

Jourdon, A., Le Pourhiet, L., Mouthereau, F., & Masini, E. (2019). Role of rift maturity on the architecture and shortening distribution in mountain belts. *Earth and Planetary Science Letters*, *512*, 89–99. https://doi.org/10.1016/j.epsl.2019.01.057

Keyser, W., Tsai, C., Iizuka, Y., Oberhänsli, R., & Ernst, W. G. (2016). High-pressure metamorphism in the Chinshuichi area, Yuli belt, eastern Taiwan. *Tectonophysics*, *692*, 191–202. https://doi.org/10.1016/j.tecto.2015.09.012

Lacombe, O., Mouthereau, F., Angelier, J., & Deffontaines, B. (2001). Structural, geodetic and seismological evidence for tectonic escape in SW Taiwan. *Tectonophysics*, *333*(1–2), 323–345. https://doi.org/10.1016/S0040-1951(00)00281-X

Lahfid, A., Beyssac, O., Deville, E., Negro, F., Chopin, C., & Goffé, B. (2010). Evolution of the Raman spectrum of carbonaceous material in low-grade metasediments of the Glarus Alps (Switzerland). *Terra Nova*, *22*(5), 354–360. https://doi.org/10.1111/j.1365-3121.2010.00956.x

Lee, J. C., Angelier, J., Chu, H. T., Yu, S. B., & Hu, J. C. (1998). Plate-boundary strain partitioning along the sinistral collision suture of the Philippine and Eurasian plates: Analysis of geodetic data and geological observation in southeastern Taiwan. *Tectonics*, *17*(6), 859–871. https://doi.org/10.1029/98TC02205

Lee, Y.-H., Byrne, T., Wang, W.-H., Lo, W., Rau, R.-J., & Lu, H.-Y. (2015). Simultaneous mountain building in the Taiwan orogenic belt. *Geology*, *43*(5), 451–454. https://doi.org/10.1130/G36373.1

Lee, Y. H., Chen, C. C., Liu, T. K., Ho, H. C., Lu, H. Y., & Lo, W. (2006). Mountain building mechanisms in the Southern Central Range of the Taiwan Orogenic Belt: From accretionary wedge deformation to arc-continental collision. *Earth and Planetary Science Letters*, *252*(3–4), 413–422. https://doi.org/10.1016/j.epsl.2006.09.047

Lester, R., McIntosh, K., Van Avendonk, H. J. A., Lavier, L., Liu, C. S., & Wang, T. K. (2013). Crustal accretion in the Manila trench accretionary wedge at the transition from subduction to mountain-building in Taiwan. *Earth and Planetary Science Letters*, *375*, 430–440. https://doi.org/10.1016/j.epsl.2013.06.007

Letouzey, J., & Kimura, M. (1986). The Okinawa Trough: Genesis of a back-arc basin developing along a continental margin. *Tectonophysics*, *125*(1–3), 209–230. https://doi.org/10.1016/0040-1951(86)90015-6

Li, C. F., & Song, T. R. (2012). Magnetic recording of the Cenozoic oceanic crustal accretion and evolution of the South China Sea basin. *Chinese Science Bulletin*, *57*(24), 3165–3181. https://doi.org/10.1007/s11434-012-5063-9

Li, C.-F., Xu, X., Lin, J., Sun, Z., Zhu, J., Yao, Y., et al. (2014). Ages and magnetic structures of the South China Sea constrained by deep tow magnetic surveys and IODP Expedition 349. *Geochemistry, Geophysics, Geosystems*, *15*, 4958–4983. https://doi.org/10.1002/2014GC005567

Li, J. B., Ding, W. W., Wu, Z. Y., Zhang, J., & Dong, C. Z. (2012). The propagation of seafloor spreading in the southwestern subbasin, South China Sea. *Chinese Science Bulletin*, *57*(24), 3182–3191. https://doi.org/10.1007/s11434-012-5329-2

Lin, A. T., Watts, A. B., & Hesselbo, S. P. (2003). Cenozoic stratigraphy and subsidence history of the South China Sea margin in the Taiwan region. *Basin Research*, *15*(4), 453–478. https://doi.org/10.1046/j.1365-2117.2003.00215.x

Lin, C. (2000). Thermal modeling of continental subduction and exhumation constrained by heat flow and seismicity in Taiwan. *Tectonophysics*, *324*, 189–201. https://doi.org/10.1046/j.1365-2117.2003.00215.x

Lin, C., Harris, R., Sun, W., & Zhang, G. (2019). Geochemical and geochronological constraints on the origin and emplacement of the East Taiwan ophiolite. *Geochemistry, Geophysics, Geosystems*, *20*, 2110–2133. https://doi.org/10.1029/2018GC007902

Lin, C.-H. (2002). Active continental subduction and crustal exhumation: The Taiwan orogeny. *Terra Nova*, *14*(4), 281–287.

Lin, K.-C., Hu, J.-C., Ching, K.-E., Angelier, J., Rau, R.-J., Yu, S.-B., et al. (2010). GPS crustal deformation, strain rate and seismic activity after the 1999 Chi-Chi earthquake in Taiwan. *Journal of Geophysical Research*, *115*, B07404. https://doi.org/10.1029/2009JB006417

Liou, J. G., & Ernst, W. G. (1984). Summary of Phanerozoic metamorphism in Taiwan. *Memoir of the Geological Society of China*, *6*, 133–152.

Liu, T., Hsieh, S., Chen, Y., & Chen, W. (2001). Thermo-kinematic evolution of the Taiwan oblique-collision mountain belt as revealed by zircon fission track dating. *Earth and Planetary Science Letters*, *186*, 45–56.

Lo, C.-H., & Onstott, T. C. (1995). Rejuvenation of K-Ar systems for minerals in the Taiwan Mountain Belt. *Earth and Planetary Science Letters*, *131*, 71–98.

Lo, C. H., & Yui, T. F. (1996). $^{40}Ar/^{39}Ar$ dating of high-pressure rocks in the Tananao Basement Complex, Taiwan. *Journal of Geological Society of China-Taiwan*, *39*, 13–30.

Lock, J. (2007). Interpreting low-temperature thermochronometric data in fold-and-thrust belts: An example from the Western Foothills, Taiwan. University of Washington, Taiwan, 68(11).

Malavieille, J. (2010). Impact of erosion, sedimentation, and structural heritage on the structure and kinematics of orogenic wedges: Analog models and case studies. *GSA Today*, *20*(1), 4–10. https://doi.org/10.1130/GSATG48A.1

Malavieille, J., & Trullenque, G. (2009). Consequences of continental subduction on forearc basin and accretionary wedge deformation in SE Taiwan: Insights from analogue modeling. *Tectonophysics*, *466*(3–4), 377–394. https://doi.org/10.1016/j.tecto.2007.11.016

Marchadier, Y., & Rangin, C. (1990). Polyphase tectonics at the southern tip of the Manila trench, Mindoro-Tablas Islands, Philippines. *Tectonophysics*, *183*(1–4), 273–287. https://doi.org/10.1016/0040-1951(90)90421-4

McIntosh, K., van Avendonk, H., Lavier, L., Lester, W. R., Eakin, D., Wu, F., et al. (2013). Inversion of a hyper-extended rifted margin in the southern Central Range of Taiwan. *Geology*, *41*(8), 871–874. https://doi.org/10.1130/G34402.1

Mesalles, L., Lee, Y.-H., Ma, T.-C., Tsai, W.-L., Tan, X.-B., Lee, H.-Y. (2019). A Late-Miocene Yuli Belt? New constraints on the eastern Central Range depositional ages. TAO. https://doi.org/10.3319/TAO.2019.06.24.01

Mesalles, L., Mouthereau, F., Bernet, M., Chang, C. P., Lin, A. T. S., Fillon, C., & Sengelen, X. (2014). From submarine continental accretion to arc-continent orogenic evolution: The thermal record in southern Taiwan. *Geology*, *42*(10), 907–910. https://doi.org/10.1130/G35854.1

Mouthereau, F., Angelier, J., & Lee, J. C. (2001). Le séisme du 21 septembre 1999: Influence de l'héritage structural et implication du socle au front de la chaîne de Taiwan. *Comptes Rendus de l'Academie de Sciences - Serie IIa: Sciences de La Terre et Des Planetes*, *333*(1), 93–103. https://doi.org/10.1016/S1251-8050(01)01616-0

Mouthereau, F., Deffontaines, B., Lacombe, O., & Angelier, J. (2002). Variations along the strike of the Taiwan thrust belt: Basement control on structural style, wedge geometry, and kinematics. Geological Society of America Special Papers, 31–54.

Mouthereau, F., Fillon, C., & Ma, K. F. (2009). Distribution of strain rates in the Taiwan orogenic wedge. *Earth and Planetary Science Letters*, *284*(3–4), 361–385. https://doi.org/10.1016/j.epsl.2009.05.005

Mouthereau, F., & Lacombe, O. (2006). Inversion of the Paleogene Chinese continental margin and thick-skinned deformation in the Western Foreland of Taiwan. *Journal of Structural Geology*, *28*(11), 1977–1993. https://doi.org/10.1016/j.jsg.2006.08.007

Page, B. M., & Suppe, J. (1981). Page and Suppe, 1981.pdf. *American Journal of Science*, *281*, 195–227.

Pautot, G., Rangin, C., Briais, A., Tapponnier, P., Beuzart, P., Lericolais, G., et al. (1986). Spreading Direction in the Central South China Sea. *Nature*, *321*, 150–154.

Pelletier, B. (1985). De la fosse de Manille à la chaîne de Tai?wan: Etude géologique aux confins d'une subduction et d'une collision actives.

Pelletier, B., Cotten, J., Bellon, H., Bassoulet, C., & Stephan, J. F. (1986). Field setting, petrography, chemistry, K-Ar ages and origin of the magmatic and sedimentary associated rocks of the Hengchun peninsula, southern Taiwan. *Bulletin of the Central Geological Survey*, *4*, 27–54.

Pelletier, B., & Stephan, J. F. (1986). Middle Miocene obduction of collision registered in the Hengchun Peninsula: Geodynamic implications for the evolution of Taiwan. *Tectonophysics*, *125*, 133–160.

Pelletier, B., Stephan, J. F., Blanchet, R., Muller, C., & Hu, H. N. (1985). L'emergence d'une zone de collision active a la pointe sud de Taiwan (peninsule d'Hengchun); tectoniques superposees et mise en evidence d'une obduction miocene moyen. *Bulletin de La Société Géologique de France*, *1*(2), 161–171. https://doi.org/10.2113/gssgfbull.I.2.161

Pinet, N., & Cobbold, P. R. (1992). Experimental insights into the partitioning of motion within zones of oblique subduction. *Tectonophysics*, *206*(3–4), 371–388. https://doi.org/10.1016/0040-1951(92)90388-M

Pinet, N., & Stephan, J. F. (1990). The Philippine wrench fault system in the Ilocos Foothills, northwestern Luzon, Philippines. *Tectonophysics*, *183*(1–4), 207–224. https://doi.org/10.1016/0040-1951(90)90417-7

Pubellier, M., Ali, J., & Monnier, C. (2003). Cenozoic Plate interaction of the Australia and Philippine Sea Plates: "Hit-and-run" tectonics. *Tectonophysics*, *363*(3–4), 181–199. https://doi.org/10.1016/S0040-1951(02)00671-6

Pulver, M. H., Crespi, J. M., & Byrne, T. B. (2002). Lateral extrusion in a transpressional collision zone: An example from the pre-Tertiary metamorphic basement of Taiwan. *Geological Society of America Special Paper*, *358*, 107–120. https://doi.org/10.1130/0-8137-2358-2.107

Sarewitz, D. R., & Karig, D. E. (1986). Processes of allochthonous terrane evolution, Mindoro Island, Philippines. *Tectonics*, *5*(4), 525–552. https://doi.org/10.1029/TC005i004p00525

Shellnutt, J. G., & Hsieh, R. B.-J. (2016). Mantle potential temperature estimates of basalt from the East Taiwan ophiolite. *Terrestrial, Atmospheric and Oceanic Sciences*, *27*(6), 853–863. https://doi.org/10.3319/TAO.2016.05.24.01(TT)

Shyu, J., Sieh, K., & Chen, Y. (2005). Tandem suturing and disarticulation of the Taiwan orogen revealed by its neotectonic elements. *Earth and Planetary Science Letters*, *233*(1–2), 167–177. https://doi.org/10.1016/j.epsl.2005.01.018

Shyu, J. B. H., Sieh, K., Avouac, J.-P., Chen, W.-S., & Chen, Y.-G. (2006). Millennial slip rate of the Longitudinal Valley fault from river terraces: Implications for convergence across the active suture of eastern Taiwan. *Journal of Geophysical Research*, *111*, B08403. https://doi.org/10.1029/2005JB003971

Shyu, J. B. H., Sieh, K., Chen, Y. G., Chuang, R. Y., Wang, Y., & Chung, L. H. (2008). Geomorphology of the southernmost Longitudinal Valley fault: Implications for evolution of the active suture of eastern Taiwan. *Tectonics*, *27*, TC1019. https://doi.org/10.1029/2006TC002060

Shyu, J. B. H., Sieh, K., Chen, Y. G., & Liu, C. S. (2005). Neotectonic architecture of Taiwan and its implications for future large earthquakes. *Journal of Geophysical Research*, *110*, B08402. https://doi.org/10.1029/2004JB003251

Sibuet, J.-C., Letouzey, J., Barbier, F., Charvet, J., Foucher, J.-P., Hilde, T. W. C., et al. (1987). Back arc extension in the Okinawa Trough. *Journal of Geophysical Research*, *92*(B13), 14,041–14,063. https://doi.org/10.1029/JB092iB13p14041

Simoes, M., Avouac, J. P., Beyssac, O., Goffe, B., Farley, K. A., & Chen, Y. (2007). Mountain building in Taiwan: A thermokinematic model. *Journal of Geophysical Research*, *112*, B11405. https://doi.org/10.1029/2006JB004824

Simoes, M., Beyssac, O., & Chen, Y. G. (2012). Late Cenozoic metamorphism and mountain building in Taiwan: A review. *Journal of Asian Earth Sciences*, *46*, 92–119. https://doi.org/10.1016/j.jseaes.2011.11.009

Suppe, J. (1981). Mechanics of mountain building and metamorphism in Taiwan. *Memoir of the Geological Society of China*, *4*, 67–89.

Tang, C.-C., Zhu, L., Chen, C.-H., &Teng, T.-L. (2011). Significant crustal structuralvariation across the Chaochou Fault, southern Taiwan: New tectonicimplications for convergent plate boundary. *Journal of Asian Earth Science*, *41*(6), 564–570.

Taylor, B., & Hayes, D. E. (1980). The tectonic evolution of the South China Basin. In *The Tectonic and Geologic Evolution of Southeast Asian Seas and Islands, Geophysical Monograph Series* (pp. 89–104). Washington, DC: American Geophysical Union. https://doi.org/10.1029/GM023p0089

Teng, L. S. (1996). Extensional collapse of the northern Taiwan mountain belt. *Geology*, *24*(10), 949. https://doi.org/10.1130/0091-7613(1996)024<0949:ECOTNT>2.3.CO;2

Teng, S. L., Wang, Y., Tang, C. H., Huang, C. Y., Huang, T. C., Yu, M. S., & Ke, A. (1991). Tectonic aspects of the Paleogene depositional basin of northern Taiwan. *Proceedings of the Geological Society of China*, *34*, 313–336.

Tensi, J., Mouthereau, F., & Lacombe, O. (2006). Lithospheric bulge in the West Taiwan Basin. *Basin Research*, *18*(3), 277–299. https://doi.org/10.1111/j.1365-2117.2006.00296.x

Teyssier, C., Tikoff, B., & Markley, M. (1995). Oblique plate motion and continental tectonics. *Geology*, *23*(5), 447–450. https://doi.org/10.1130/0091-7613(1995)023<0447:OPMACT>2.3.CO;2

Tillman, K. S., & Byrne, T. B. (1995). Kinematic analysis of the Taiwan Slate Belt. *Tectonics*, *14*(2), 322–341.

Tsai, C., Iizuka, Y., & Ernst, W. G. (2013). Diverse mineral compositions, textures, and metamorphic *P–T* conditions of the glaucophane-bearing rocks in the Tamayen mélange, Yuli belt, eastern Taiwan. *Journal of Asian Earth Sciences*, *63*, 218–233. https://doi.org/10.1016/j.jseaes.2012.09.019

Vidal, O., & Parra, T. (2000). Exhumation paths of high-pressure metapelites obtained from local equilibria for chlorite-phengite assemblages. *Geological Journal*, *35*, 139–161.

Wang, K., & Hu, Y. (2006). Accretionary prisms in subduction earthquake cycles: The theory of dynamic Coulomb wedge. *Journal of Geophysical Research*, *111*, B06410. https://doi.org/10.1029/2005JB004094

Willett, S. D. (1999). Orogeny and orography: The effects of erosion on the structure of mountain belts. *Journal of Geophysical Research*, *104*(B12), 28,957–28,981. https://doi.org/10.1029/1999JB900248

Willett, S. D., Fisher, D., Fuller, C., Yeh, E. C., & Lu, C. Y. (2003). Erosion rates and orogenic-wedge kinematics in Taiwan inferred from fission-track thermochronometry. *Geology*, *31*(11), 945–948. https://doi.org/10.1130/G19702.1

Wiltschko, D. V., Hassler, L., Hung, J.-H., & Liao, H. S. (2010). From accretion to collision: Motion and evolution of the Chaochou Fault, southern Taiwan. *Tectonics*, *29*. https://doi.org/10.1029/2008TC002398

Wintsch, R. P., & Li, X.-H. (2014). Hf and O isotopic evidence for metamorphic crystallization of zircon during contact metamorphism of Fenniaolin metabasalts, Tananao complex, Taiwan. *Lithos*, *205*, 142–147. https://doi.org/10.1016/j.lithos.2014.06.011

Wu, J., Suppe, J., Lu, R., & Kanda, R. (2016). Philippine Sea and East Asian plate tectonics since 52 Ma constrained by new subducted slab reconstruction methods. *Journal of Geophysical Research: Solid Earth*, *121*, 4670–4741. https://doi.org/10.1002/2016JB012923

Yamato, P., Mouthereau, F., & Burov, E. (2009). Taiwan mountain building: Insights from 2-D thermomechanical modelling of a rheologically stratified lithosphere. *Geophysical Journal International*, *176*(1), 307–326. https://doi.org/10.1111/j.1365-246X.2008.03977.x

Yu, S., Chen, H., & Kuo, L. (1997). Velocity field of GPS stations in the Taiwan area. *Tectonophysics*, *274*, 41–59.

Yumul, G. P., Dimalanta, C. B., Tamayo, R. A., & Maury, R. C. (2003). Collision, subduction and accretion events in the Philippines: A synthesis. *The Island Arc*, *12*(2), 77–91. https://doi.org/10.1046/j.1440-1738.2003.00382.x

Zhang, X., Cawood, P. A., Huang, C. Y., Wang, Y., Yan, Y., Santosh, M., et al. (2016). From convergent plate margin to arc–continent collision: Formation of the Kenting Mélange, southern Taiwan. *Gondwana Research*, *38*, 171–182. https://doi.org/10.1016/j.gr.2015.11.010

Zhao, M., Qiu, X., Xia, S., Xu, H., Wang, P., Wang, T. K., et al. (2010). Seismic structure in the northeastern South China Sea: *S*-wave velocity and V_P/V_S ratios derived from three-component OBS data. *Tectonophysics*, *480*(1–4), 183–197. https://doi.org/10.1016/j.tecto.2009.10.004